Electroacupuncture at Governor Vessel improves neurobehavioral function via silencing complexin I

Yang Xu (asdfxy@qq.com)
Department of Anesthesiology

Jia Liu
Institute of Neuroscience, Laboratory Zoology Department. Kunming Medical University, Kunming, China

Yang Xu
Institute of Neurological Disease, Department of Anesthesiology, Translational Neuroscience Center, West China Hospital, Sichuan University

Liu-Ling Xiong
Institute of Neurological Disease, Department of Anesthesiology, Translational Neuroscience Center, West China Hospital, Sichuan University & The Research Units of West China, Chinese Academy of Med

Cui-Yun Li
Institute of Neuroscience, Laboratory Zoology Department. Kunming Medical University, Kunming, China

Ya Jiang
Institute of Neuroscience, Laboratory Zoology Department. Kunming Medical University, Kunming, China

Yang-Yang Wang
Institute of Neurological Disease, Department of Anesthesiology, Translational Neuroscience Center, West China Hospital, Sichuan University

Ting-Hua Wang
West China Hospital of Sichuan University

Article

Keywords: Governor Vessel electro-acupuncture, neurobehavioral function, CPLX1, SCC

Posted Date: July 15th, 2020

DOI: https://doi.org/10.21203/rs.3.rs-37066/v1

Electroacupuncture at Governor Vessel improves neurobehavioral function via silencing complexin I

Yang Xu[1], Jia Liu[2], Xiao-Ming Zhao[1], Liu-Ling Xiong[1], Cui-Yun Li[2], Ya Jiang[2], Yang-Yang Wang[1], and Ting-Hua Wang[1,2*]

[1] Institute of Neurological Disease, Department of Anesthesiology, Translational Neuroscience Center, West China Hospital, Sichuan University & The Research Units of West China, Chinese Academy of Medical Sciences, Chengdu 610041, China

[2] Institute of Neuroscience, Laboratory Zoology Department. Kunming Medical University, Kunming, China

Correspondence and requests for materials should be addressed to T.W. (email: tinghua_neuron@263.net)

Abstract

Governor Vessel electro-acupuncture (GV), as a traditional Chinese medicine, has been proved that it can reduce scar and promote axon regeneration. However, the underlying mechanism remains unclear. Herein, complexin I (CPLX1), as a candidate protein involved in the process of GV treatment on spinal cord contusion (SCC), was found by using protein chip. Therefore, using a CRISPR/Cas9 knockout approach, we silenced CPLX1 to assess its role in the process of GV treatment. Additionally, eIF5A1 promotes translation of CPLX1 with PPG sequence, we attempt to uncover whether eIF5A1 play a role in GV treatment. Indeed, GV can reduce scar and promote axon regeneration after SCC. $CPLX1^{-/+}$ SCC rats demonstrated that decreased CPLX1 improved the microenvironment of injured area via reducing the components of fibrotic scar and further enhanced the synaptic plasticity, which benefit the regeneration of axons. And eIF5A1 could regulate the expression of CPLX1 in the process of GV treatment. Therefore, GV contributes to axon regeneration and synapse plasticity via eIF5A1 regulating CPLX1 following SCC, providing a convincible mechanism for improving the therapeutic efficacy of GV for SCC.

Introduction

Spinal cord contusion (SCC), which causes profound and persistent neurological deficits, induces clinically irreversible disability and results in a large number of comorbidities (1, 2). Those complications are characterized by neurological deficits and motor dysfunction caused by demyelination of axons and cellular death (3). Terribly, it is estimated that only half of affected patients regain supraspinal control of movements below the level of the lesion after spinal cord injury (SCI) (2). The scar tissue that forms at the SCI site plays an important role in sealing the lesion and inhibiting axon regeneration (4, 5). This scar tissue can be classified into two types: glial and fibrotic scar (6). The glial scar often surrounds the central core (fibrotic scar) that refers to the astrogliotic region and prevents non-CNS cells (such as leukocytes) from invading the CNS parenchyma (7). For years the glial scar has been widely regarded as the main impediment for regenerating axons attempting to reach their distal targets (8). However, recent research shows that contrary to prevailing dogma, astrocyte scar formation aids rather than prevents CNS axon regeneration (9). The fibrotic scar, comprising a dense extracellular matrix, is originated from multiple interacting stromal cells including NG2 glia/oligodendrocyte precursor cells (OPCs), meningeal and/or vascular derived fibroblasts, pericytes, ependymal cells, and phagocytic macrophages (8). There's growing evidence that the fibrotic scar is the major impediment for axonal regeneration. Previous studies attempt to eliminate or modify the specific fibrotic components, which has shown potential to improve axonal regeneration. However, there are many different extracellular matrix molecules and stromal cells deposited in the fibrotic scar. Numerous inhibitory cues present in the scar makes molecule-specific targeting strategies impractical (10). Therefore, there still is a lack of effective therapeutic strategies for the treatment of SCC.

Governor Vessel electro-acupuncture (GV), as a therapeutic technique used in traditional Chinese medicine, is a type of therapy with the purpose of producing synthetic electric and needling stimulation (11). It has been reported that GV application not only rescues the death of neural cells (12), but also improves median nerve function

by somatotopically distinct neuroplasticity (13). In addition, evidence from both clinical trials and basic researches supports that GV can restore the motor function, bladder function, and sensory function after SCI, resulting in promising functional recovery (14-17). Given the satisfactory therapeutic effects, it was urgent to find the therapeutic mechanism of GV on the treatment of SCC.

Here, we hypothesized that GV could regulate neural specific proteins expression involved in the process of GV to promote neuroprotection and recovery after SCC. The protein expression profile of spinal cord segments in both SCC and GV treated models was analyzed by using protein mass spectrometry analysis. The identified proteins included the molecules related to nervous system development, neurogenesis and wounding, such as solute carrier family 12 member 5 (Slc12a5), sodium- and chloride-dependent glycine transporter 2 (Slc6a5), sodium- and chloride-dependent GABA transporter 3 (Slc6a11), excitatory amino acid transporter 2 (Slc1a2) and complexin I (CPLX1). Further experiments discovered that CPLX1 may be neural specific proteins involved in the process of GV treatment on SCC. CPLX1 is a presynaptic small molecule protein consisting of 134 amino acids, forming a SNARE complex with synaptobrevin, syntaxin, and snap25 in the central nervous system, involving in anchoring, pre-excitation, and fusion of axonal end vesicles (18). Moreover, CPLX1 is highly homologous hydrophilic protein that is tightly conserved, with 100% identity among mouse, rat, and human. Studies demonstrate that CPLX1 is significantly down-regulated in AD patients, which is positively correlated with the severity of this disease (19). Additionally, CPLX1 is still at a low level in the medial thalamus of Wernicke's encephalopathy, suggesting that it may contribute to the pathophysiology of thalamic damage (20). Moreover, loss of CPLX1 induces abnormalities in long-term potentiation (21, 22). In the field of central nervous system (CNS) injury, changes of CPLX1 expression after SCI have been proved by numerous studies (23-25). In the light of the above, CPLX1 may play a critical role in the process of GV treatment on SCC. But, the underlying mechanism remains largely unknown.

In this study, we delete CPLX1 to assess the role of CPLX1 in GV treatment using a CRISPR/Cas9 knockout approach. Additionally, eIF5A1 stimulate the translation of

CPLX1 with PPG sequence (26, 27), we attempt to uncover whether eIF5A1 play a role in the GV treatment. Herein, we provide evidence that GV promote the recovery of motor function via regulating CPLX1 using immunofluorescence double labeling analysis, western blot (WB), electromyography (EMG), motor evoked potential (MEP), field potential, diffusion tensor imaging (DTI), and Golgi staining. Taken together, these data evidence the efficacy of GV on the treatment for SCC and demonstrate the underlying mechanism in the process of GV treatment on SCC, establishing a reliable molecular theoretical basis for clinical application of GV in the treatment of SCI.

Results

GV effectively improves the hindlimb motor dysfunction in SCC rats via increases synaptic plasticity through changing the axon components and transporter activity. As GV is a clinically feasible way to improve the motor dysfunction effectively, we aimed to decipher its distinct cellular actions. First, Basso, Beattie, and Bresnahan (BBB) scores of GV application group increased gradually since the 4th week post injury (wpi), suggesting that GV effectively improves hindlimb motor dysfunction in SCC rats (Figure 1A). Two weeks after SCC, we found that the hematoma is disappearing gradually and the scar formed closes the injury site (Supplemental Figure 1A). GV treatment reduce the scar formation showing a small scar area (Figure 1, B and C, and Supplemental Figure 1, A and B). Interestingly, less formation of cavity and inflammatory cell infiltration were observed after GV treatment (Figure 1B). We next examined whether GV treatment may alleviate the collapse of micro-structures. Data of electron microscopy (EM) in Figure 1C showed significant protection of myelinated axons within the injured spinal cord of GV treated rats (Figure 1, D and E). Additionally, GV treatment significantly increased the percentage of presynaptic coverage of motor neurons after spinal cord injury (Figure 1, D and F). These data suggested that GV treatment increase the axonal plasticity.

To acquire mechanistic insight, we performed protein mass spectrometry analysis of spinal cord injured segments at 4wpi after GV treatment. We identified 379 proteins that were differentially expressed including 226 up-regulated and 153 down-regulated

proteins (false discovery rate [FDR]-adjusted $p<0.05$, fold change >2 or <0.5) (Figure 1G). Gene Ontology (GO) enrichment analysis of differentially expressed genes (DEGs) were conducted in three categories including biological process (BP), cellular component (CC) and molecular function (MF). Results demonstrated that almost DEGs locate in axon and synapse except extracellular space (Figure 1H). Transporter activity was the top enriched term in MF. While for BP, neurogenesis and neurotransmitter transport belonging to the top ten enriched term were focused (Figure 1H). Moreover, DEGs were selected again according the category of fold change >5 or <0.2 to further analysis these differentially expressed proteins. 23 up-regulated and 16 down-regulated proteins were picked (Figure 1I). Then, venny 2.1.0 software was used to uncover the overlapping proteins which have striking differences and participate in focused MF and BP. A total of 5 up-regulated proteins (Slc12a5, Slc6a5, Slc6a11, Slc1a2 and Cplx1) were selected (Figure 1J).

Moderate reduction of CPLX1 significantly improves the motor function for a relatively stable time after SCC even better than GV-treatment. It is well known that, excepting the scarring, axon growth inhibitory factors are the other key impediment to regenerating axons, in which chondroitin sulfate proteoglycans (CSPGs) is one of the major components (28). Here, the effective function of five candidate proteins to promote the axon elongation were uncovered under an inhibitory environment in which CSPGs was added. Groups of slc6a11-siRNA and CPLX1-siRNA significantly restored the potential of axon growth when neurons grow in an inhibitory environment (Figure 2, A and B). And, down-regulation of CPLX1 showed even more growth potential. Therefore, we next examined the role of CPLX1 in the process of GV treating SCC rats. As the axon trajectory of interneuron populations can vary and thus play different roles in different sites near a SCC, so we first determined whether neurons responded differently according to their location relative to the lesion site, and tissues in rostral, lesion and caudal sites were separated to do further analyze. First, CPLX1 significantly increased in the rostral and caudal sites comparing with epicenters at different time points (Supplemental Figure 1, C and D). The comparison

assessed by WB in the same sites was made between the SCC and GV-SCC group demonstrating that the CPLX1 expression of rostral and caudal segments significantly decreased after GV treated group comparing to the SCC group (Figure 2C). Thus, these implied that silencing CPLX1 expression may be the reason for the effectiveness of GV treatment.

For further researching, we used a transgenic rat line with homozygous knockout of CPLX1 generated by CRISPR/Cas9 gene editing system. Due to $CPLX1^{-/-}$ rats had a profound ataxia and short lifespan, $CPLX1^{-/+}$ rats were used for the following experiment, which have been verified with significant levels of CPLX1 gene silencing (Supplemental Figure 2). Then, $CPLX1^{-/+}$ and GV-WT group of SCC models were conducted for further investigating. Reduced CPLX1 expression in SCC models resulted in significant improvements in hindlimb moving ability within the first 3 weeks. However, in GV-treated rats, functional recovery first appeared by 4 weeks and became significant gradually. This trend of those two groups kept extending even at 9, 10, 11 week, on those period no GV carry out, indicating the functional sustainability in the GV treating and partial delection of CPLX1 in SCC rats (Figure 2D). When the nervi ischiadicus was stimulated near the base of the tail in WT rats, little or no reflex was evoked in the segmental gastrocnemius muscle EMG recordings, regardless of the stimulation current intensity or rate of stimulation. However, the response was more obvious in the $CPLX1^{-/+}$ and GV-WT group as shown in the results that the amplitudes of $CPLX1^{-/+}$ group ($P<0.01$) and GV-WT ($P<0.05$) were larger than the WT group (Figure 2, H and I). Besides, the MEP recordings of the WT SCC rats remained stable and the evaluated measures showed steady and similar values for the duration of the testing period. The amplitude of $CPLX1^{-/+}$ group ($P<0.01$) and GV-WT ($P<0.05$) was larger than the WT group. The latency in the $CPLX1^{-/+}$ group was larger when compared to the WT group (Figure 2, E-G).

Moderate reduction of CPLX1 ($CPLX1^{-/+}$) enhances neural tissue regeneration and reduces fibrotic scar tissue after SCC even more than GV application. As previously mentioned, reduction of CPLX1 using genetic method in the SCC models

significantly ameliorated the motor dysfunction. Eleven weeks later, the content of CPLX1 at the rostral and caudal spinal cord extraction in the CPLX1$^{-/+}$ SCC models was lower than that of WT SCC group, respectively (Figure 3A). Further, Diffusion tensor imaging (DTI) scans was used noninvasively to longitudinally track neural tissue regeneration progress, which was an ideal measurement for both human and animal SCI studies. Different colors of tracking were used to mark the direction of fiber orientations. Results demonstrated that spinal cord neural regeneration was more obvious in CPLX1$^{-/+}$ SCC rats. But, in the WT rats, the ascending and descending blue fiber tracks were disconnected, leaving a gap on the center region of the spinal cord. While after GV treatment, no gap existed in the spinal cord, and the blue fiber signals filled the whole spinal cord structure. Quantitative analyses of percentage of rostral–caudal voxels and fractional anisotropy (FA) values indicated a higher value in GV-WT and CPLX1$^{-/+}$ groups compared with WT group, which demonstrated significant neural tissue regeneration in CPLX1$^{-/+}$ rats and GV-treated models (Figure 3B).

Function changes of caudal spinal cord to the lesion side play a key role in the recovery of motor function. Immunofluorescence double labeling revealed that fiber scars are mainly distributed in the lesion core but glial scars are mostly localized in the rostral and caudal regions (penumbra) (Supplemental Figure 3A). But, GV treatment increased the GFAP positive area largely in the lesion core and decreased fibrotic scar marked by laminin and fibronectin when comparing to SCC group at 4wpi (Supplemental Figure 3, A-E). Furthermore, quantities analyses showed that the protein levels of fibronectin and laminin were higher in the SCC group than that of GV-SCC and sham group (Supplemental Figure 3, F-H). When the GV treatment was performed for 8 weeks and unapplied for 3 weeks, fibronectin- and laminin-positive fibrotic scar areas in the dorsal spinal cord were significantly reduced compared to WT SCC group (Figure 3, D-F). Reduced level of laminin and fibronectin after GV revealed that the fiber scar decreased and an advantageous environment conducive to axonal regeneration or plasticity enhancement formed. While, in CPLX1$^{-/+}$ SCC rats, fibronectin- and laminin-positive fibrotic scar tissue barely existed and their positive area were lower than GV-WT group (Figure 3, D-F). These changes were also

confirmed by WB results (Figure 3, G and H).

Moderate reduction of CPLX1 (CPLX1$^{-/+}$) increases synaptic plasticity and promotes axon regrowth through highly expressing the GAP43. Further, we wondered that whether the scar-reducing effect also promotes spinal circuitry caudal to the lesion through increasing synaptic plasticity. To assess this, Golgi-stain was carried out for quantifying a fine details of neuron morphology for motor neurons located throughout the caudal ventral horn. Data showed that the dendritic spine density of CPLX1$^{-/+}$ SCC group was larger than GV and WT SCC groups (Figure 4, A and B). For the dendritic length, CPLX1$^{-/+}$ SCC group was statistically longer than WT (Figure 4, A and C). However, there was barely difference in the number of dendritic branch (Figure 4, A and D). We next tested whether the increase in synaptic plasticity noted at the caudal to the injury epicenter was associated with synaptogenesis. Double stain of anti-synapsin I and anti-Beta-Tubulin III (Tuj1) was performed to quantify changes in presynaptic coverage on lumbar ventral horn motor neurons. There were significant main effects for both genotype (WT vs. CPLX1$^{-/+}$, $P<0.000$) and different treatments (CPLX1$^{-/+}$ vs. GV-WT, $P<0.05$) (Figure 4, E and F, and Supplemental Figure 4). Results of synapse in the lamellae 9 to 10 of ventral horns of spinal cords also confirmed the synaptogenesis using transmission electron microscope (Supplemental Figure 5, A and B). The synapse covered more in the groups of CPLX1$^{-/+}$ SCC ($P<0.0001$) and GV-WT SCC ($P<0.05$) than the WT SCC group (Supplemental Figure 5, A and B). Besides, demyelination was more obvious in the SCC group but it was significantly improved when treating with GV or partial delection of CPLX1 (Supplemental Figure 5, A and C). Moreover, decreased CPLX1 expression promoted axon growth even when these neurons were in an environment that fully with the inhibitory molecules including Nogo-A, Semaphorin3A (Sema-3A) and CSPGs, abundant at the spinal cord lesion core (Figure 4, G and H). For the spinal cord neurons, moderate reduction of CPLX1 also played the same effect (Supplemental Figure 6). Which protein was attributed to this effect? We detected the distribution of growth associated protein 43 (GAP43) which was significantly up-regulated in CPLX1$^{-/+}$ cortical neurons than that of the WT group

at both axon and some (Figure 4, I and M).

Moderate reduction of CPLX1 (CPLX1$^{-/+}$) elevates serotonergic innervation and field excitatory postsynaptic potential (fEPSP). Previously, increased serotonergic innervation strongly modulate the recovery of motor function after SCI (29). We then tested whether the scar-reducing effect also promotes axon regrowth of serotonergic spinal axons. Indeed, the CPLX1$^{-/+}$ SCC rats showed increased density of 5-HT^{+} axons innervating the ventral horn caudal to the lesion compared to WT SCC animals (Figure 5, A and B). And GV administration also enhanced the 5-HT^{+} fibers compared with that of WT SCC models (Figure 5, A and B). Same trends also happened in the longitudinal section of the WT, GV-WT and CPLX1$^{-/+}$ SCC groups (left side of white dotted line showed the caudal side to the lesion core) (Figure 5A).

To further investigate whether regenerated axons and enhanced synaptic plasticity were functional, fEPSP was measured in the caudal spinal cord to the injury, which may reflect the recovery of motor function of hindlimbs. Data indicated that field EPSP was consistently evoked in all three groups. For the slope in the groups of GV-WT SCC and CPLX1$^{-/+}$ SCC, they were higher than WT respectively ($P<0.01$), and in the amplitude of GV-WT ($P<0.001$) and CPLX1$^{-/+}$ ($P<0.05$), they were higher than WT SCC group, while no obvious difference was observed in the response latency (Figure 5, C-F).

GV improves the neurological deficits via eIF5A1 regulating the expression of CPLX1. From the above, we proved that decreased CPLX1 expression has a special contribution on the effectiveness of GV treatment. We then assessed whether other molecule involved in this process. Protein sequence of CPLX1 is highly conserved in rattus norvegicua, mus musculus and homo sapiens, and they all had the same PPG sequences which induce ribosomes become stalled resulting no full-length product produced (Figure 6A). However, previously reports demonstrate that eukaryotic eIF5A1 can rescue the stalled ribosomes (30, 31). To verify whether eIF5A1 was the main reason for down-regulated CPLX1 in the process of GV treatment, we firstly used the primary cultured cortical neurons to verify the action of eIF5A1 to regulate the

translation and function of CPLX1. After overexpressing eIF5A1, the level of eIF5A1 increased, followed by the increasing of CPLX1 level. While eIF5A1 was down-regulated with the decreasing expression of CPLX1, and there was a reduction eIF5A1 when CPLX1 was overexpressed (Figure 6, B and D). These observations suggested that eIF5A1 can positively promote the expression of CPLX1. For the functional validation, FM1-43 dye was used to label and then monitor synaptic vesicles, secretory granules and other endocytic structures in a variety of preparations. When stimulating with high potassium (K^+), the intensity of FM1-43 fluorescence in CPLX1 siRNA and eIF5A1 siRNA group were higher than other groups (Figure 6, E and F). However, the high signal phenomenon of eIF5A1 siRNA was reversed after overexpressing CPLX1 (Figure 6, E and F). Results also demonstrated decreased exocytosis in neurons with lower-expressing of CPLX1. To further verify this, we examined potassium (K^+) and calcium (Ca^{2+}) fluxes in neurons using microelectrode ion flux estimation (MIFE). Before stimulating, K^+ flux of CPLX1$^{-/+}$ neurons was higher than that of WT neurons ($P<0.05$), while there was a significant reduction of the flux of CPLX1$^{-/+}$-eIF5A1-ORF after overexpressing eIF5A1 ($P<0.001$) (Figure 6, G and H). Accordingly, the flux of Ca^{2+} in the CPLX1$^{-/+}$ group was much less than that of WT group ($P<0.01$), but after overexpressing eIF5A1, the flux of Ca^{2+} was increased obviously ($P<0.05$) (Figure 6, I and J). Delection of CPLX1 (CPLX1$^{-/-}$) also significantly decreased the efflux of Ca^{2+}, which can be rescued by overexpressing CPLX1 but not eIF5A1 (Figure 6K).

To evaluate whether eIF5A1-dependent CPLX1 expression can affect the neurobehavioral recovery after SCC, we used CPLX1$^{-/+}$ rats to generate SCC model and HSV- eIF5A1-ORF was injected into the spinal cord lesion area of CPLX1$^{-/+}$ rats. WB results confirmed that the content of CPLX1 was decreased as mentioned above in CPLX1$^{-/+}$ SCC group compared to WT SCC group ($P<0.001$), but increased after over-expression of eIF5A1 in CPLX1$^{-/+}$ SCC group ($P<0.05$) (Figure 7A). EMG recordings of these SCC models demonstrated that over-expression of eIF5A1 reverses the enhancement of amplitudes in CPLX1$^{-/+}$ SCC group ($P<0.05$) (Figure 7, B and C). Same trends also found in the MEP recordings in which the amplitude of CPLX1$^{-/+}$ group was larger than WT group ($P<0.01$) and CPLX1$^{-/+}$-eIF5A1-ORF group ($P<0.05$) (Figure 7,

D and E). And, the response latency in the CPLX1$^{-/+}$ group was shorter when compared to the CPLX1$^{-/+}$-eIF5A1-ORF group ($P<0.01$) (Figure 7F). BBB scores analysis showed that CPLX1$^{-/+}$-eIF5A1-ORF group had a lower BBB scores compared to CPLX1$^{-/+}$ SCC models begin 4wpi, revealing that over-expression of eIF5A1 in CPLX1$^{-/+}$ SCC models reversed the improved neurobehavioral defects (Figure 7G). We finally investigated whether the motor function recovery and amelioration after GV treatment was due to down-regulated CPLX1 through eIF5A1. HSV- eIF5A1-ORF was injected into the spinal cord lesion area of WT SCC models whose were given the GV treatment. Six weeks later, BBB scores of GV+ eIF5A1-ORF group was lower than that of GV-WT group (Figure 7H). The protein levels of eIF5A1 and CPLX1 were increased in the lesion area of GV+ eIF5A1-ORF group comparing with GV-SCC group (Figure 7, I-K).

Discussion

SCI induces widespread molecular and biochemical changes including altered mRNA and protein expression, axonal plasticity, and neuronal cell death, and there is no cure for drugs and methods. Nowadays, GV is widely used in the treatment of SCI (32, 33). However, the mechanism of GV on neurogenesis is still largely unknown, which seriously limit its approval and application. Herein, we verified the therapeutic effect of GV treatment on SCC rats. BBB scores showed that SCC rats get a remarkable motor recovery after GV application. Besides, less formation of cavity, inflammatory cell infiltration, demyelination and increased synaptic plasticity were found after GV treatment. Using protein chip, CPLX1 was found to be the neural specific protein in the process of GV application. The level of CPLX1 was reduced after GV performed. In addition, we confirmed that lower CPLX1 expression promoted axon regeneration and synapse plasticity and motor function in vivo. Therefore, axon regeneration and synapse plasticity appear both contributing to the functional recovery, revealing a possible mechanism that GV application promote function recovery of SCC models. Moreover, the observation of sequence PPG containing in CPLX1 requires eIF5A1 to rescue their translation providing further investigation.

Previous studies have demonstrated that scarring represents a major barrier for axonal regrowth, and moderate inhibition of this process will enable axonal regrowth and improve functional recovery (34). In this study, fibrotic scar tissue rich in fibronectin and laminin formed at the lesion site after SCC, which is the key impediment for regenerate axons, containing axon growth inhibitory factors including chondroitin sulfate proteoglycans (CSPGs) (5). Furthermore, reduced level of laminin and fibronectin after GV treatment which assessed by immunofluorescence double labeling revealed that the fiber scar decreased and an advantageous environment conducive to axonal regeneration or plasticity enhancement formed. It was previously reported that secondary degeneration of neurons is reduced and axon regeneration is facilitated by GV treatment (35). Besides, modulating the plastic changes at the spinal cord level play an important role in improving functional recovery (36). In this study, DTI was performed to track spinal cord neural regeneration progress. The fiber signals filled the whole spinal cord structure in a continuously state after GV application, which proved that GV could promote the axon regeneration (37). In summary, GV can facilitate axon regeneration and improve recovery of motor function.

In order to investigate the underlying mechanism, results of protein chip show that the expression of CPLX1 decreased obviously after GV treatment. CPLX1 is a highly charged protein that is essential for Ca^{2+}-mediated neurotransmission that appears to act by interacting with and regulating the SNAREs (38). To date, CPLX1 levels are differentially expressed in many psychiatric and neurodegenerative disorders (39). Studies have shown that CPLX1 is specifically existed in the nervous system and pancreatic B cells, and expressed in neurons, microglia, and astrocytes, especially mainly expressed in the synaptic structure-rich region (18). In recent years, it has been found that CPLX1 is a molecule with two-way regulation function, which exerts both positive and negative effects on vesicle exocytosis, facilitating synchronous neurotransmission while inhibiting spontaneous fusion events (40, 41). Moreover, CPLX1 is crucially involved in neurological development and neurotransmitter release. The availability and importance of CPLX1 in nerve repair have been expounded in many studies (42). Given the important role of CPLX1 in nervous system, we want to

ascertain whether GV treatment effectively improves motor function of SCC rats through down-regulation of CPLX1. Indeed, CPLX1$^{-/+}$ rats had a better motor recovery as revealed by higher BBB scores and increased EMG and MEP signals. The objectivity of SEP and MEP recording ensures that lower expression of CPLX1 enhances the electrophysiological conduction through the injured spinal cord and the excitability of the sciatic nerve, which further confirm the BBB scores obtained (43).

Numerous evidences show that the dendritic spines can change shape, size, and number following various injuries (44, 45). GV treatment also promotes synaptic plasticity via regulating CPLX1. After SCI, there is an acute reduction in dendritic number in these survived neurons with rapid dendritic atrophy. Meanwhile, spontaneous dendritic plasticity could reflect a compensatory response of the spinal cord to the functional deficits caused by the injury (45, 46). Increased dendritic spine density observed in neurons have entered into a more plastic state, which indicate availability to form new synapses (47). Indeed, data in the current report indicate that low expression of CPLX1 can increase the dendritic spine density and dendritic length in the caudal site to the epicenter. Other reports demonstrate that dendritic plasticity is formed through actin cytoskeleton reorganization which responds to glutamate release regulate downstream signals such as proteinkinase A (PKA), proteinkinase C (PKC) and mitogen-activated protein kinase (MAPK) through activating aminomethylphosphonic acid (AMPA) and N Methyl D Aspartate (NMDA) receptors (44). As CPLX1 plays an important role in the process of neurotransmitters release (48), thus enhanced the synaptic plasticity of neurons may result from the low expression of CPLX1 clamping chaotic release of neurotransmitters caused by SCI.

As yet, one of the important strategies for treating SCC is to promote axon regeneration in the epicenter (49). Data demonstrated that decreased CPLX1 expression promoted axon regrowth even when neurons were incubated in an inhibitory environment through highly up-regulation of GAP43 involving in axonal growth and regeneration (25, 50). We then investigated whether GV treatment promotes regrowth of descending axons in vivo, which mediate voluntary motor movement, important for locomotion (10). Increased serotonergic (5-HT) axons play a key role in activating and

modulating lumbar motor circuitry after GV treatment (51). Previously studies report that 5-HT axons have an intrinsic ability to sprout and grow after SCI, bypassing the epicenter and repopulating gray matter caudal to the injury site, which has been implicated in spontaneous recovery of motor function (51, 52). Here, the density 5-HT$^+$ axons caudal to the epicenter enhanced in SCC rats either deficient in CPLX1 (CPLX1$^{-/+}$) or performed the GV treatment. Moreover, the regrowth of 5-HT$^+$ axons repopulate lumber spinal cord gray matter showing a topographically appropriate pattern around the anterior motor neurons. Field potential demonstrated that the regenerated descending axons across the lesion and activated the intraspinal circuits below the lesion contributing to the majority of functional recovery (53). Here, myelination of survived axons increased in the group of low expression of CPXL1 and GV treatment, suggesting that these axons could conduct action potentials. These evidences demonstrated that regenerated axons and enhanced synaptic plasticity caused an increased fEPSP, promoting the recovery of motor function in rats with SCC. Further conclusion is that GV treatment promotes the recovery of spinal cord injury, which may be related to the involvement of CPLX1 in axon regeneration and synaptic plasticity.

In particular, CPLX1 is a highly conserved protein with the sequences PPG, which can stall the translation. Moreover, many researches have confirmed that eIF5A1 can rescue the translation of sequences PPG (26, 27), so we made an assumption that eIF5A1 can regulate CPLX1 in the response to the neurobehavioral deficits in SCC. In this study, we proved that eIF5A1 can positively regulate the expression of CPLX1 protein. The regulatory verification of SCC function recovery *in vitro* and release of neuronal vesicle neurotransmitters *in vivo* was carried out, indicating that overexpression of CPLX1 can reverse neuronal vesicle release dysfunction caused by eIF5A1 interference. On the other hand, overexpression of eIF5A1 can reverse the recovery of motor function and better fiber remodeling caused by CPLX1 silencing.

Altogether, our results present a convincible mechanism for further exploring CPLX1 silencing through GV administration as a practical and promising clinical strategy for addressing SCC repair.

Methods

Animals and materials

Adult female Sprague-Dawley rats (200-250g) were obtained from animal center of Sichuan University. All procedures were followed by international, national and institutional guidelines and were approved by local authorities (Sichuan Medical Experimental Animal Care Commission #2016098A). Animals were housed in a comfortable and clean condition under a 12/12h dark-light cycle following SCC experiment, and food was available ad libitum. Moreover, their bladders were manually massaged three times daily. Complexin1 knock-out rats were provided by Institute of laboratory animal sciences, CAMS&PUMC. HSVs was obtained from Brain VTA.

Rat model of Spinal Cord Contusion (SCC)

After deeply anesthetized with a ketamine (80mg/kg, i.p.)/xylazine (10mg/kg, i.p.) mixture, rats were fixed in a prone position. A midline skin incision was made between the area of T10 and L2, and then paravertebral muscles were separated. After exposing the spinal cord, the vertebrae were stabilized with clamps and the rats were suffered a moderate (75kdyn) mid-thoracic (T10) contusion SCI (PCI3000 Precision Cortical Impactor, Hatteras Instruments, Inc). While in the sham group, the rats only exposed the spinal cord without contusion after anesthetized. After impaction, the surgery incision was sutured and rats were hydrated with 2 ml of saline (intraperitoneal injection) and were given prophylactic antibiotic (0.1ml cefotaxime sodium, i.p.) for 3 days. Manual bladder expression was performed 3 times a day until recovery of micturition reflex.

Basso, Beattie, and Bresnahan (BBB) Score

The recovery of motor function in hind limbs was evaluated using a Basso, Beattie, and Bresnahan open field locomotion rating scoring system (BBB score). BBB score was performed on weekly after injury. In brief, this scale used for assessing hindlimb function includes evaluation standards ranging from a score of 0, indicating no spontaneous movement, to a maximum score of 21, with an increasing score indicating

the use of individual joints, coordinated joint movement, coordinated limb movement, weight-bearing, and other functions. Three researchers ‘‘blinded’’ to rat treatment status performed 5min tests on all animals.

MRI data acquisition

All MRI research was accomplished with a 7.0 Tesla MR scanner (Bruker Biospec 70/30, Ettlingen, Germany). Structural and functional images of spinal cord were acquired with a spine coil, which received MRI and DTI signals from the spinal cord. Each rat was anesthetized with 3% isflurone before MRI scan, and anesthesia was maintained during the scan by continuous administration of mixture gas (2% isflurone –O_2/N_2 (30%:70%)). During MRI, the temperature, heart rate and breathe of rats was monitored periodically. The images were captured with T2 weighted image (T2WI) sequence (time repetition (TR) / echo time (TE) = 2000ms/15ms, field of view (FOV) =50mm×50mm, Rare Factor=8). DTI was performed after MRI. Echo planar imaging sequence was applied with 15 gradient directions (b=1000s/mm^2, TE=32.2ms, Segments=8, TR/TE=2000ms/32.2ms, FOV=25mm × 25mm, matrix =128 × 128). After obtaining the image, each data was corrected using DTI studio (Jiang *et al.*, 2006). Then the Diffusion Toolkit software was used to perform white matter fiber tracking on the corrected DTI data and display the image using Trackvis (http://www.trackvis.org).

DTI data processing

DTI scans were processed and analyzed by means of dedicated mricron software (http://people.cas.sc.edu/rorden/mricron/install.html), and DTI Studio (http://cmrm.med.jhmi.edu/). The deformation field is calculated in the same way for each of all diffusion-weighted (DW) scans and applied accordingly. Afterwards, diffusion Toolkit (https://www.trackvis.org) was performed to track matter fiber. After processing, three vertical eigenvalues are derived from each pixel to calculate b0 images and FA. The direction of the eigenvector associated with the largest eigenvalue is set to the main direction of the local neural fiber. The background removal threshold of 0.10 was set to exclude non-normal voxels and any significant noise; the smoothing

of the interpolating fiber was set to 20% and the minimum fiber length was set to 1cm for continuous fiber reconstruction. The FA values in the region of interest (ROI) at the rostral, lesion and caudal sites were extracted and used for statistical comparison.

MEP

After being anaesthetized by 3% isoflurane, the limbs of rats were abducted and fixed on a board by cloth bands. Successive stimulation was given at musculi hippicus, and the recorded contraction of the target muscle was taken at the stimulating intensity between 3.5 and 12mA. A pulse train of 5 pulses was used, with pulse width 100s, intra-pulse period of 50ms, and inter-train frequency of 0.5 Hz. The MEP signal was recorded for 500ms after the initiation of each pulse-train, but only the portion of the MEP signal located within 50ms of the final stimulus pulse was analyzed. These stimulation frequencies were chosen through reference to papers by (54). MEP was recorded from each of the limbs using sub-dermal needle electrode pairs. The grand average of all time-locked sweeps was taken and then was used for all further analysis.

EMG

After anesthetized by 3% isflurone, the upper back of each rat was shaved and cleaned and a small skin incision was made in the motor area of cerebral cortex to allow placement of the transmitter. The wire electrodes of the transmitter were tunneled subcutaneously to the right hindlimb by separating the skin from the muscle layer using blunt dissection. EMG recordings were made from rats to track the changes that occurred in reflexes over time.

Field potential

Horizontal spinal cord slices were prepared according to the previous reports (55). Briefly, Horizontal slices (300μm thick) were cut using a vibrating microtome (VT1200 S, Leica Biosystems, Germany) submerged in oxygenated, ice-cold, sucrose-substituted artificial cerebrospinal fluid (sACSF) (in mM): 250 sucrose, 2.5 KCl, 1 $CaCl_2$, 6 $MgCl_2$, 25 $NaHCO_3$, 11 glucose and 1 NaH_2PO_4 (PH 7.4). Then the slice was immediately

transferred to a recovery bath and perfused with oxygenated containing ACSF (in mM): 118 NaCl, 2.5 KCl, 2.5 $CaCl_2$, 1 $MgCl_2$, 25 $NaHCO_3$, 1 NaH_2PO_4, 11 glucose and pH 7.4 with NaOH. The slice was positioned in the bath, and secured under a custom-made net. The sections were held around 270mV by injecting a hyperpolarisation current, and the spike was elicited by a 500pA depolarising ramp current for 100ms. Recordings were made at 37℃ using an Axopatch 200B amplifier (Molecular Devices, Sunnyvale, CA, USA). Data were collected (sampled at 50 kHz, filtered between 2 and 10kHz) and analysed on a computer using pCLAMP 10 software (Molecular Devices Corp., Sunnyvale, CA 94089 USA).

Tissue Harvest

Animals performed for WB were deeply anesthetized. After rats were decapitated, the spinal cord tissues rostral and caudal to the lesion site were fetched quickly and were placed into phosphate buffered saline (PBS) at 4℃ for following experiments. For immunofluorescent staining, the samples were collected after intracardiac perfusion with 50 ml physiological saline followed with 4% paraformaldehyde. Additionally, the tissue samples for Golgi staining should be collected instantly after anaesthetizing rats. After removal, the surface blood was quickly washed away with H_2O_2, and the samples were soaked in the immersion liquid.

HE Staining

Firstly, frozen sections were washed by distilled water for 2 min, and then were stained using hematoxylin and eosin. After rinsing in tap water for 10 min to wash off any excess staining solution followed by distilled water once more and 0.95% ethanol for 5 seconds, sections were counterstained with Eosin, dehydrated, cleared with xylene and mounted with neutral gum. The stained sections were observed using OlyVIA slice scanner to detect morphologic changes.

Primary neuronal cultures

Neonatal rats (less than 24 hours) were used for primary neuron culture. Animals were

decapitated at the base of the foramen magnum after sterilization, brain and spinal cord tissues were harvested, minced, and isolated by 0.25% trypsinase for 10min at 37°C following by DMEM with 10% BSA to neutralize the effect of trypsinase. The cells were collected by centrifugation at 1,000 rpm for 10 min, resuspended, and plated in 6-well plates (Corning, USA) at the density of 10^5 cells/ml. After incubation at 37 °C with 5% CO2 for 4 h, the culture medium previously used was replaced by neuronal seeding medium, which consisted of Neurobasal Medium (21103049, Gibco) added with B27(17504044, Gibco). To achieve gene silencing, dissociated neurons were transfected with various nucleic acid molecules (siRNA-NC (siRNA Control), Slc12a5-siRNA，Slc6a5-siRNA, Slc6a11-siRNA, Slc1a2-siRNA and CPLX1-siRNA) using riboFECT CP Transfection Reagent (C10511-05, RIBOBIO).

Lenti-virus Transection in spinal cord neurons

Six days later, neurons were transfected by HSV virus containing different open reading frame (ORF) (HSV-CPLX1-ORF and HSV-eIF5A1-ORF) with MOI=1. Then, images were acquired using Leica AF6000 at 3 days after transfection. . Five fields were used for measuring soma size and number as well as neurite length of cortical neurons by using Leica DMI6000B (LAS AF system) and mean value was calculated. Then, the size, number, and neurite length were measured, respectively.

Synaptic bouton activity (FM1-43)

After clearing the supernatant in the cultured primary neuron, primary neuron was washed twice with PBS. Cells were incubated for 10 minutes in a 2ml low-K^+ buffer, then were incubated for 5 minutes in high-K^+ buffer containing 10mM FM1-43 dye, followed by washing with a low-K^+ buffer to remove the surface-bound dye. Later, cells were stimulated for 5 minutes in a high-K^+ medium at 37°C. The extra liquid was removed and formaldehyde was used to fix. Images were captured using a Leica TCS SP5 microscope equipped with a HCX PL APO 63X 1.4 numerical aperture oil immersion objective.

Ultrastructural analysis

Sections were cut from the tissues of spinal cord using an ultramicrotome (Leica EM FC7), and then placed on formva-coated grids. Ultrathin sections were examined in a FEI Tecnai G2 F20 transmission electron microscope at 80kV. Images were acquired by camera (EagleTM4K CCD). Myelinated and degenerating axons were counted from 3 different fields of the damaged penumbra for each sample. Synaptogenesis was analyzed from 3 different fields of the lamellae 9 to 10 of ventral horns of spinal cords. 3 sections per rat were counted. All the analyses were performed in a blinded condition.

Ion-selective flux measurements

Complete experimental procedure of microelectrode ion flux estimation (MIFF) has been processed by a modified procedures according to the previously reports (56). Cortical neurons for the MIFE detections were cultured for 6 days at 5×10^5 cells/well on coverslips coated with poly-L-lysine. Cells were washed in ASCF (0.5mM $CaCl_2$, 5mM KCl, 52mM NaCl, 26.2mM $NaHCO_3$, 0.9mM NaH_2PO_4, 0.5mM MgCl2, 5mM D-Glucose, 2mM HEPES, PH 7.4) and then placed into a measuring chamber immerged into 2ml ASCF. Measurements were performed after three days post transfected with different HSV virus. The K^+ and Ca2+ fluxes were recorded for 5mins prior to the addition of a high-K^+ solution (250mM KCl, 0.2mM $CaCl_2$, 52mM NaCl, 26.2mM $NaHCO_3$, 0.9mM NaH_2PO_4, 0.5mM MgCl2, 5mM D-Glucose, 2mM HEPES, PH 7.4), and recordings continued for 15 min once the testing liquid (0.2mM $CaCl_2$, 0.2mM KCl, 52mM NaCl, 26.2mM $NaHCO_3$, 0.9mM NaH_2PO_4, 0.5mM MgCl2, 5mM D-Glucose, 2mM HEPES, PH 7.4) was immediately added to exchange the high-K^+ solution. For recording the K^+ and Ca^{2+} fluxes, microelectrodes were filled with 100mM KCl and 100mM $CaCl_2$, respectively. Data was collected at a rate of 10 samples/sec and averaged over 6 second intervals. Net ion fluxes ($nmolm^{-2}s^{-1}$) were analyzed and calculated using MIFE software.

Immunocytochemistry

After animals were perfused with 4% paraformaldehyde solution, spinal cord segments

were harvested and dehydrated by 30 % sucrose overnight. Sagittal sections (1cm) were prepared by using freezing microtome (Leica CM1900, Germany) encompassing regions both rostral and caudal to the lesion. For cell immunofluorescence, neurons were fixed with 4% paraformaldehyde solution. Slides and cells were washed three times with PBS followed by blocking in a mixture of 5% normal goat serum (NGS) and 0.1% Triton X-100 in PBS. After blocking, specimens were incubated in primary antibody diluted in 2% NGS overnight at 4°C. Primary antibodies for slides were mouse anti-GFAP (1:200, #MAB 3402, Chemicon), mouse anti-Tuj1 (1:200, #MAB1195, R&D systems), rabbit anti-laminin (1:100, #ab11575, Abcam), rabbit anti-fibronectin (1:200, #ab2413, Abcam) and rabbit anti-5HT (1:50, #ab10385, Abcam), and rabbit anti-synapsin I (1:500, #SAB4502904, Sigma-Aldrich). Primary antibodies for neurons were mouse anti-Tuj1 (1:200, #MAB1195, R&D systems), rabbit anti-GAP43 (1:400, #5307, CST), and rabbit anti-synapsin I (1:500, #SAB4502904, Sigma-Aldrich). The next day, the sections were washed extensively with PBS and incubated in the appropriate secondary antibody overnight (goat anti-rabbit IgG H&L (Alexa Fluor® 488) (1:200, #ab150077, Abcam) and goat anti-mouse IgG H&L (Alexa Fluor® 594) (1:200, ab150116, Abcam)). After extensive washing, the sections were stained with DAPI and viewed with a confocal microscope (Zeiss, Germany). Pixel intensity was measured on images taken on a standard fluorescent microscope (Leica) with a uniform exposure setting and analyzed using ImageJ.

Western Blotting

Protein was extracted from frozen spinal cord tissue samples (200mg), then lysed and homogenized in RIPA lysis buffer containing 2 % of cocktail pill (Roche). All samples were centrifuged at 12000 ×g for 10 min at 4°C. Then the total supernatant protein was collected and its concentration was determined by BCA protein assay (Thermo ScientificTM, #23225). After separating samples containing 80μg of protein on 10% sodium dodecyl sulfate polyacrylamide gel electrophoresis, the separated proteins were transferred onto PVDF membranes, and the membranes were blocked for 1 h with TBST buffer containing 5% skim milk. Membranes were incubated overnight at 4 °C

with the following primary antibodies, rabbit anti-CPLX1 (1:1000, #17700, SCT); rabbit anti-Laminin (1:1000, #ab11575, Abcam); rabbit anti-Fibronectin (1:5000, #ab2413, Abcam), then were incubated for 2h at room temperature with Horseradish peroxidase-coupled secondary antibodies: goat anti-rabbit IgG H&L(HRP)(1:10000, #205718, Abcam). GAPDH was used as a loading control (1:50000, #AC033, Abclonal). All samples were visualized using ECL detection reagents (Beyotime, China).

Golgi Staining

Golgi Staining was performed using the FD Fast Golgi Staining Kit (#PK401, FD NeuroTechnologies, Inc.) according to the protocol. The spinal cord tissues were soaked in the mixture of solution A and B for 3weeks, and then transfer into solution C for 72 h in dark place. Then the fixed tissues were sectioned at a thickness of 100um at -22°C using a thermostated microtome (CM1860, Leica). Tissues were stained followed by rinsing with double distilled water for 4mins, three times. Later, sections were placed in the mixture (1x D, 1x E and 2x distilled water) for 10 min. After repeating washing with distilled water twice, sections were dehydrated in 50%, 75%, and 95% and absolute ethanol for 4 minutes, soaked in xylene and mounted with neutral gum. The image was taken using an OlyVIA 2.9 slice scanner (OLYMPUS).

Statistics

All data in the experiment are presented as mean ± standard deviation. Measurement data were statistically analyzed utilizing SPSS 21.0 software (SPSS, Inc., Chicago, USA). Student's t-test was used for statistics between 2 groups. Three or more groups of data were analyzed by one-way ANOVA. $P<0.05$ was regarded as statistically significant.

Reporting summary.

Further information on experimental design is available in the Nature Research Reporting Summary linked to this article.

Data availability

The data that support the findings of this study are available from the corresponding author upon reasonable request.

References

1. Moraud EM, et al. Mechanisms Underlying the Neuromodulation of Spinal Circuits for Correcting Gait and Balance Deficits after Spinal Cord Injury. *Neuron*. 2016;89(4):814-28.
2. Asboth L, et al. Cortico-reticulo-spinal circuit reorganization enables functional recovery after severe spinal cord contusion. *Nature neuroscience*. 2018;21(4):576-88.
3. Wang X, et al. Recovery from chronic spinal cord contusion after Nogo receptor intervention. *Annals of neurology*. 2011;70(5):805-21.
4. Chen B, et al. Reactivation of Dormant Relay Pathways in Injured Spinal Cord by KCC2 Manipulations. *Cell*. 2018;174(3):521-35.e13.
5. Ruschel J, Bradke F. Systemic administration of epothilone D improves functional recovery of walking after rat spinal cord contusion injury. *Experimental neurology*. 2018;306:243-9.
6. Zhu Y, Soderblom C, Krishnan V, Ashbaugh J, Bethea JR, Lee JK. Hematogenous macrophage depletion reduces the fibrotic scar and increases axonal growth after spinal cord injury. *Neurobiol Dis*. 2015;74:114-25.
7. Soderblom C, et al. Perivascular fibroblasts form the fibrotic scar after contusive spinal cord injury. *J Neurosci*. 2013;33(34):13882-7.
8. Cregg JM, DePaul MA, Filous AR, Lang BT, Tran A, Silver J. Functional regeneration beyond the glial scar. *Experimental neurology*. 2014;253:197-207.
9. Anderson MA, et al. Astrocyte scar formation aids central nervous system axon regeneration. *Nature*. 2016;532(7598):195-200.
10. Dias DO, et al. Reducing Pericyte-Derived Scarring Promotes Recovery after Spinal Cord Injury. *Cell*. 2018;173(1):153-65 e22.
11. Ding Y, et al. Electro-acupuncture promotes survival, differentiation of the bone marrow mesenchymal stem cells as well as functional recovery in the spinal cord-transected rats. *BMC*

719 *neuroscience*. 2009;10:35.
720 12. Li WJ, et al. Electro-acupuncture upregulates CGRP expression after rat spinal cord transection.
721 *Neurochemistry international*. 2012;61(8):1397-403.
722 13. Maeda Y, et al. Rewiring the primary somatosensory cortex in carpal tunnel syndrome with
723 acupuncture. *Brain : a journal of neurology*. 2017;140(4):914-27.
724 14. Liu Z, Ding Y, Zeng YS. A new combined therapeutic strategy of governor vessel electro-acupuncture
725 and adult stem cell transplantation promotes the recovery of injured spinal cord. *Current medicinal*
726 *chemistry*. 2011;18(33):5165-71.
727 15. Li M, Peng J, Song Y, Liang H, Mei Y, Fang Y. Electro-acupuncture combined with transcranial
728 magnetic stimulation improves learning and memory function of rats with cerebral infarction by
729 inhibiting neuron cell apoptosis. *Journal of Huazhong University of Science and Technology Medical*
730 *sciences = Hua zhong ke ji da xue xue bao Yi xue Ying De wen ban = Huazhong keji daxue xuebao Yixue*
731 *Yingdewen ban*. 2012;32(5):746-9.
732 16. Zhang K, et al. Electro-acupuncture promotes the survival and differentiation of transplanted bone
733 marrow mesenchymal stem cells pre-induced with neurotrophin-3 and retinoic acid in gelatin sponge
734 scaffold after rat spinal cord transection. *Stem cell reviews*. 2014;10(4):612-25.
735 17. Liu J, Wu Y. Electro-acupuncture-modulated miR-214 prevents neuronal apoptosis by targeting Bax
736 and inhibits sodium channel Nav1.3 expression in rats after spinal cord injury. *Biomedicine &*
737 *pharmacotherapy = Biomedecine & pharmacotherapie*. 2017;89:1125-35.
738 18. McMahon HT, Missler M, Li C, Sudhof TC. Complexins: cytosolic proteins that regulate SNAP
739 receptor function. *Cell*. 1995;83(1):111-9.
740 19. Nie L, et al. Ginsenoside Rg1 Ameliorates Behavioral Abnormalities and Modulates the
741 Hippocampal Proteomic Change in Triple Transgenic Mice of Alzheimer's Disease. *Oxidative medicine*
742 *and cellular longevity*. 2017;2017:6473506.
743 20. Hazell AS, Wang C. Downregulation of complexin I and complexin II in the medial thalamus is
744 blocked by N-acetylcysteine in experimental Wernicke's encephalopathy. *Journal of neuroscience*
745 *research*. 2005;79(1-2):200-7.
746 21. Freeman W, Morton AJ. Regional and progressive changes in brain expression of complexin II in a
747 mouse transgenic for the Huntington's disease mutation. *Brain research bulletin*. 2004;63(1):45-55.
748 22. Glynn D, Reim K, Brose N, Morton AJ. Depletion of Complexin II does not affect disease progression

749 in a mouse model of Huntington's disease (HD); support for role for complexin II in behavioural
750 pathology in a mouse model of HD. *Brain research bulletin*. 2007;72(2-3):108-20.
751 23. Aimone JB, Leasure JL, Perreau VM, Thallmair M, Christopher Reeve Paralysis Foundation Research
752 C. Spatial and temporal gene expression profiling of the contused rat spinal cord. *Experimental*
753 *neurology*. 2004;189(2):204-21.
754 24. Di Giovanni S, Knoblach SM, Brandoli C, Aden SA, Hoffman EP, Faden AI. Gene profiling in spinal
755 cord injury shows role of cell cycle neuronal death. *Annals of neurology*. 2003;53(4):454-68.
756 25. Merino P, Diaz A, Torre ER, Yepes M. Urokinase-type plasminogen activator (uPA) regulates the
757 expression and function of growth-associated protein 43 (GAP-43) in the synapse. *Journal of Biological*
758 *Chemistry*. 2020;295(2):619-30.
759 26. Gutierrez E, et al. eIF5A promotes translation of polyproline motifs. *Molecular cell*. 2013;51(1):35-
760 45.
761 27. Nguyen S, et al. Deoxyhypusine Modification of Eukaryotic Translation Initiation Factor 5A (eIF5A)
762 Is Essential for Trypanosoma brucei Growth and for Expression of Polyprolyl-containing Proteins. *The*
763 *Journal of biological chemistry*. 2015;290(32):19987-98.
764 28. Ruschel J, et al. Systemic Administration of Epothilone B Promotes Axon Regeneration and
765 Functional Recovery after Spinal Cord Injury. *Mol Biol Cell*. 2013;24.
766 29. Mullner A, Gonzenbach RR, Weinmann O, Schnell L, Liebscher T, Schwab ME. Lamina-specific
767 restoration of serotonergic projections after Nogo-A antibody treatment of spinal cord injury in rats. *Eur*
768 *J Neurosci*. 2008;27(2):326-33.
769 30. Doerfel LK, Wohlgemuth I, Kothe C, Peske F, Urlaub H, Rodnina MV. EF-P is essential for rapid
770 synthesis of proteins containing consecutive proline residues. *Science (New York, NY)*.
771 2013;339(6115):85-8.
772 31. Huter P, et al. Structural Basis for Polyproline-Mediated Ribosome Stalling and Rescue by the
773 Translation Elongation Factor EF-P. *Molecular cell*. 2017;68(3):515-+.
774 32. Wong AMK, Leong CP, Su TY, Yu SW, Tsai WC, Chen CPC. Clinical trial of acupuncture for patients
775 with spinal cord injuries. *Am J Phys Med Rehab*. 2003;82(1):21-7.
776 33. Mo YP, et al. Effects of Electroacupuncture at Governor Vessel Acupoints on Neurotrophin-3 in Rats
777 with Experimental Spinal Cord Injury. *Neural Plast*. 2016.
778 34. Toy D, Namgung U. Role of glial cells in axonal regeneration. *Exp Neurobiol*. 2013;22(2):68-76.

779 35. Wang Y, et al. Effects of Treatment of Treadmill Combined with Electro-Acupuncture on Tibia Bone
780 Mass and Substance PExpression of Rabbits with Sciatic Nerve Injury. *PloS one*. 2016;11(11):e0164652.
781 36. Asensio-Pinilla E, Udina E, Jaramillo J, Navarro X. Electrical stimulation combined with exercise
782 increase axonal regeneration after peripheral nerve injury. *Experimental neurology*. 2009;219(1):258-
783 65.
784 37. Feng R, Zhang F. The neuroprotective effect of electro-acupuncture against ischemic stroke in
785 animal model: a review. *African journal of traditional, complementary, and alternative medicines :*
786 *AJTCAM*. 2014;11(3):25-9.
787 38. Chen J, et al. Electro-acupuncture induced NGF, BDNF and NT-3 expression in spared L6 dorsal root
788 ganglion in cats subjected to removal of adjacent ganglia. *Neuroscience research*. 2007;59(4):399-405.
789 39. Zhou Q, et al. The primed SNARE-complexin-synaptotagmin complex for neuronal exocytosis.
790 *Nature*. 2017;548(7668):420-5.
791 40. Wragg RT, et al. Synaptic vesicles position complexin to block spontaneous fusion. *Neuron*.
792 2013;77(2):323-34.
793 41. Zdanowicz R, Kreutzberger A, Liang B, Kiessling V, Tamm LK, Cafiso DS. Complexin Binding to
794 Membranes and Acceptor t-SNAREs Explains Its Clamping Effect on Fusion. *Biophysical journal*.
795 2017;113(6):1235-50.
796 42. Ugurel E, Sehitoglu E, Tuzun E, Kurtuncu M, Coban A, Vural B. Increased complexin-1 and decreased
797 miR-185 expression levels in Behcet's disease with and without neurological involvement. *Neurological*
798 *sciences : official journal of the Italian Neurological Society and of the Italian Society of Clinical*
799 *Neurophysiology*. 2016;37(3):411-6.
800 43. Iyer S, Maybhate A, Presacco A, All AH. Multi-limb acquisition of motor evoked potentials and its
801 application in spinal cord injury. *J Neurosci Methods*. 2010;193(2):210-6.
802 44. Tan AM, Waxman SG. Spinal cord injury, dendritic spine remodeling, and spinal memory
803 mechanisms. *Experimental neurology*. 2012;235(1):142-51.
804 45. Deng LX, et al. Characterization of dendritic morphology and neurotransmitter phenotype of
805 thoracic descending propriospinal neurons after complete spinal cord transection and GDNF treatment.
806 *Experimental neurology*. 2016;277:103-14.
807 46. Horch HW, et al. Bilateral Consequences of Chronic Unilateral Deafferentation in the Auditory
808 System of the Cricket Gryllus bimaculatus. *Dev Neurosci-Basel*. 2011;33(1):21-37.

47. Alvarez VA, Sabatini BL. Anatomical and physiological plasticity of dendritic spines. *Annu Rev Neurosci*. 2007;30:79-97.

48. Kummel D, et al. Complexin cross-links prefusion SNAREs into a zigzag array. *Nat Struct Mol Biol*. 2011;18(8):927-U1603.

49. Vigneswara V, Kundi S, Ahmed Z. Receptor tyrosine kinases: molecular switches regulating CNS axon regeneration. *J Signal Transduct*. 2012;2012:361721.

50. Wu DS, et al. Intraneural Injection of ATP Stimulates Regeneration of Primary Sensory Axons in the Spinal Cord. *J Neurosci*. 2018;38(6):1351-65.

51. Freria CM, Hall JCE, Wei P, Guan Z, McTigue DM, Popovich PG. Deletion of the Fractalkine Receptor, CX3CR1, Improves Endogenous Repair, Axon Sprouting, and Synaptogenesis after Spinal Cord Injury in Mice. *J Neurosci*. 2017;37(13):3568-87.

52. Leech KA, Kinnaird CR, Hornby TG. Effects of Serotonergic Medications on Locomotor Performance in Humans with Incomplete Spinal Cord Injury. *J Neurotraum*. 2014;31(15):1334-42.

53. Deng LX, et al. A Novel Growth-Promoting Pathway Formed by GDNF-Overexpressing Schwann Cells Promotes Propriospinal Axonal Regeneration, Synapse Formation, and Partial Recovery of Function after Spinal Cord Injury. *J Neurosci*. 2013;33(13):5655-67.

54. Schlag MG, Hopf R, Redl H. Serial recording of sensory, corticomotor, and brainstem-derived motor evoked potentials in the rat. *Somatosens Mot Res*. 2001;18(2):106-16.

55. Rank MM, Flynn JR, Battistuzzo CR, Galea MP, Callister R, Callister RJ. Functional changes in deep dorsal horn interneurons following spinal cord injury are enhanced with different durations of exercise training. *J Physiol-London*. 2015;593(1):331-45.

56. Shabala L, Howells C, West AK, Chung RS. Prolonged Ab treatment leads to impairment in the ability of primary cortical neurons to maintain K+ and Ca2+ homeostasis. *Mol Neurodegener*. 2010;5.

Acknowledgements

This work was supported by grants of National Natural Science Foundation of China (NSFC) (NO.81471268 and NO.81271358) and the Key research and development projects in Sichuan province (2020YFS0043).

Author contributions

YX and THW conceived and supervised the project. JL, XMZ and LZ designed and performed the experiments together with YJ, CYL, YYW and LLX analyzed data. YX wrote the manuscript with contributions and approval of all the other authors.

Conflict of interest: The authors have declared that no conflict of interest exists.

Figure legend:

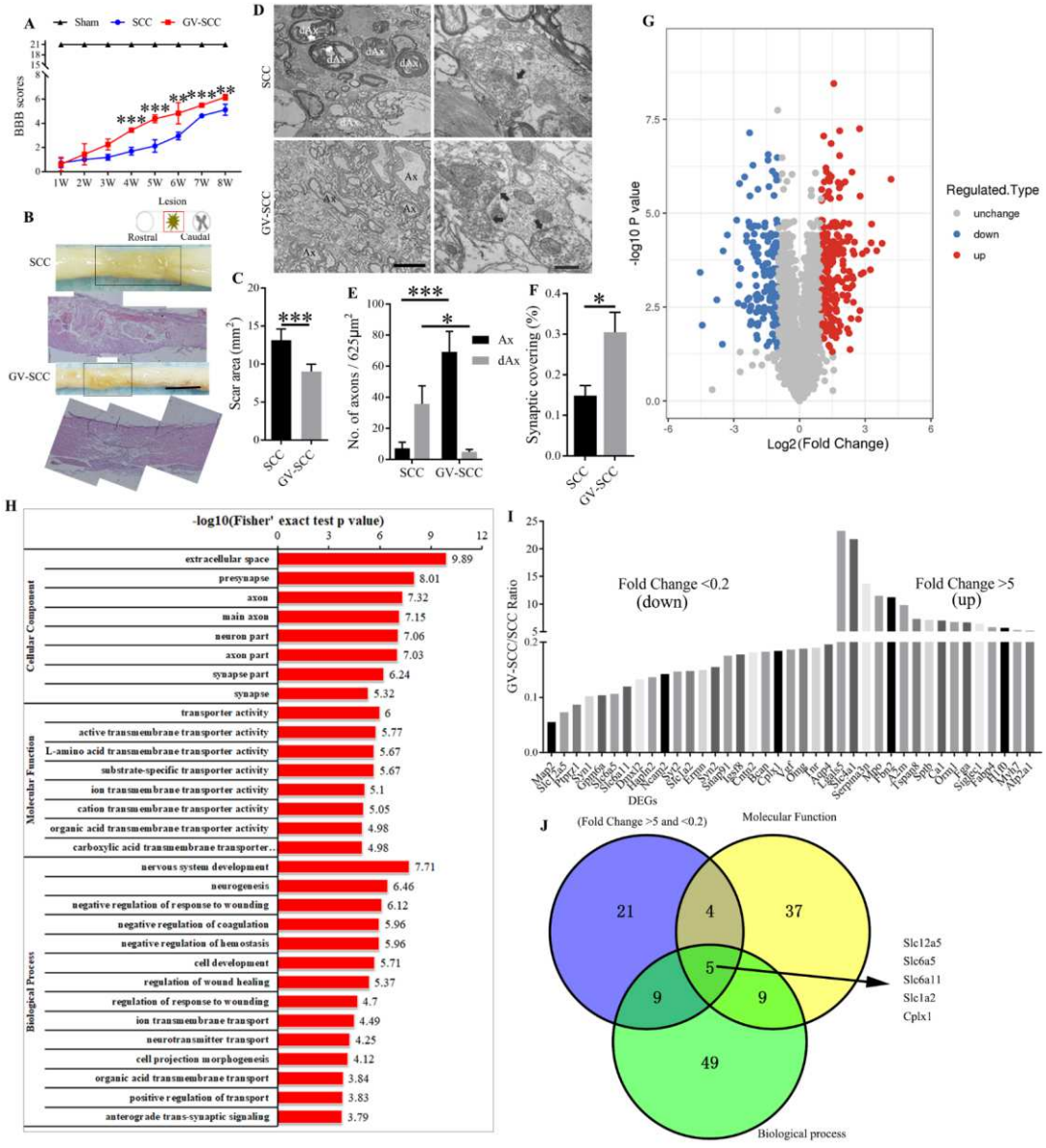

Figure 1. GV treatment accelerate the recovery of motor ability and increases synaptic plasticity after SCC which were related to down-regulating the

expression of five candidates. (**A**) BBB scores of SCC and GV-SCC groups (n = 6–8 rats per group/time point). (**B**) Low power photographs and sagittal view of the spinal cord of SCC and GV-SCC rats. Solid rectangles mark the injured area and the lower panels are the HE stain of lesion area. Scale bar: 500nm (**C**) Quantification of scar area of injured spinal cord in SCC rats with/without GV treatment (n = 6-8 mice per group). (**D**) Electron microscopic images of spinal cord sections rostral to the epicenter of the lesion in SCC rats and GV-treated rats. Arrows indicate presynaptic receptors contacting motor neuron surfaces. dAx: degenerating axon; Ax: myelinated axons. Scale bar in the left panel: 5μm； Scale bar in the right panel: 500nm. (**E**) Number of different types of axons in the damaged penumbra (n = 5 rats per group (3 sections per animal)). (**F**) Percentage of motor neuron circumference covered by synapses within ventral horn (n = 5 rats per group (3 sections per animal)). (**G**) Volcano plot of all differentially expressed genes (DEGs) between lesion sites of SCC and GV-SCC animals at 4 wpi (n = 4-6 rats per group). The data for all genes are plotted as log2 fold change of the adjusted p-value. (**H**) GO functional enrichment analysis of DEGs. (**I**) Bar graph showing the DEGs sorted according to the fold change >5 or <0.2. (**J**) Three-set venn diagram represent the selected DEGs according to the indicated strategy. Scheme in (B) indicates lesion and displayed region (red box). wpi, weeks post injury. Data were analyzed using Student's t-test. Values are plotted as means ± SEM. *P < 0.05, **P < 0.01, ***P < 0.001.

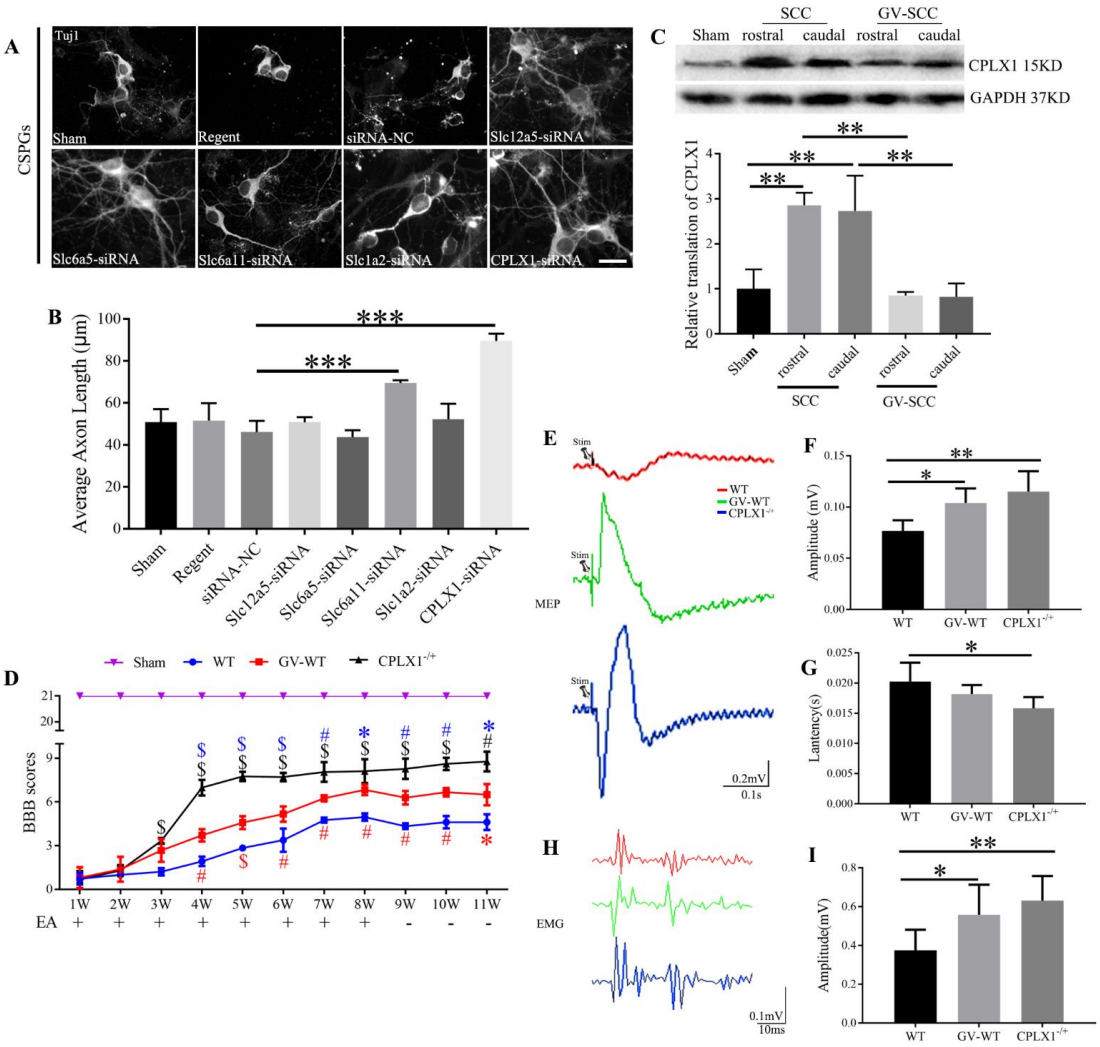

Figure 2. Moderate reduction of CPLX1 improve the MEP and EMG and enhances motor function of hind limbs simultaneously after SCC even more than GV application. (**A**) Beta-3 tubulin (Tuj-1) immunolabeling of neurons growing on inhibitory substrates (CSPGs, chondroitin sulfate proteoglycans) among different groups. Scale bar: 5μm. (**B**) Quantification of neurite length of cortical neurons under different conditions (n = 6 wells per group). (**C**) Western blots (WB) of CPLX1 in regions of rostral and caudal to the epicenter (n=3 animals per group). (**D**) BBB scores of the aforementioned experiments are shown (n=6-8 animals per group). Red symbols represent GV-WT group vs. WT group at corresponding time point; black symbols represent CPLX1$^{-/+}$ group vs. WT group at corresponding time point; Blue symbols represent CPLX1$^{-/+}$ group vs. GV-WT group at corresponding time point; *P<0.05, $^{\#}$P<0.01, $^{\$}$P<0.001. (**E**) The figure shows representative MEP signal in different group.

(**F**) Quantification and statistical analyses of amplitude for the aforementioned experiments are shown (n=4 animals per group). (**G**) Quantification of latency period for these groups (n=44 animals per group). (**H**) Representative EMG signal in different group. (**I**) Quantification of amplitude for these groups (n=4 animals per group). Data were analyzed using a one-way ANOVA followed by a Bonferroni's post hoc test. *P < 0.05, **P < 0.01, ***P < 0.001 in figure B, C, F, G and I. Values are plotted as means ± SEM.

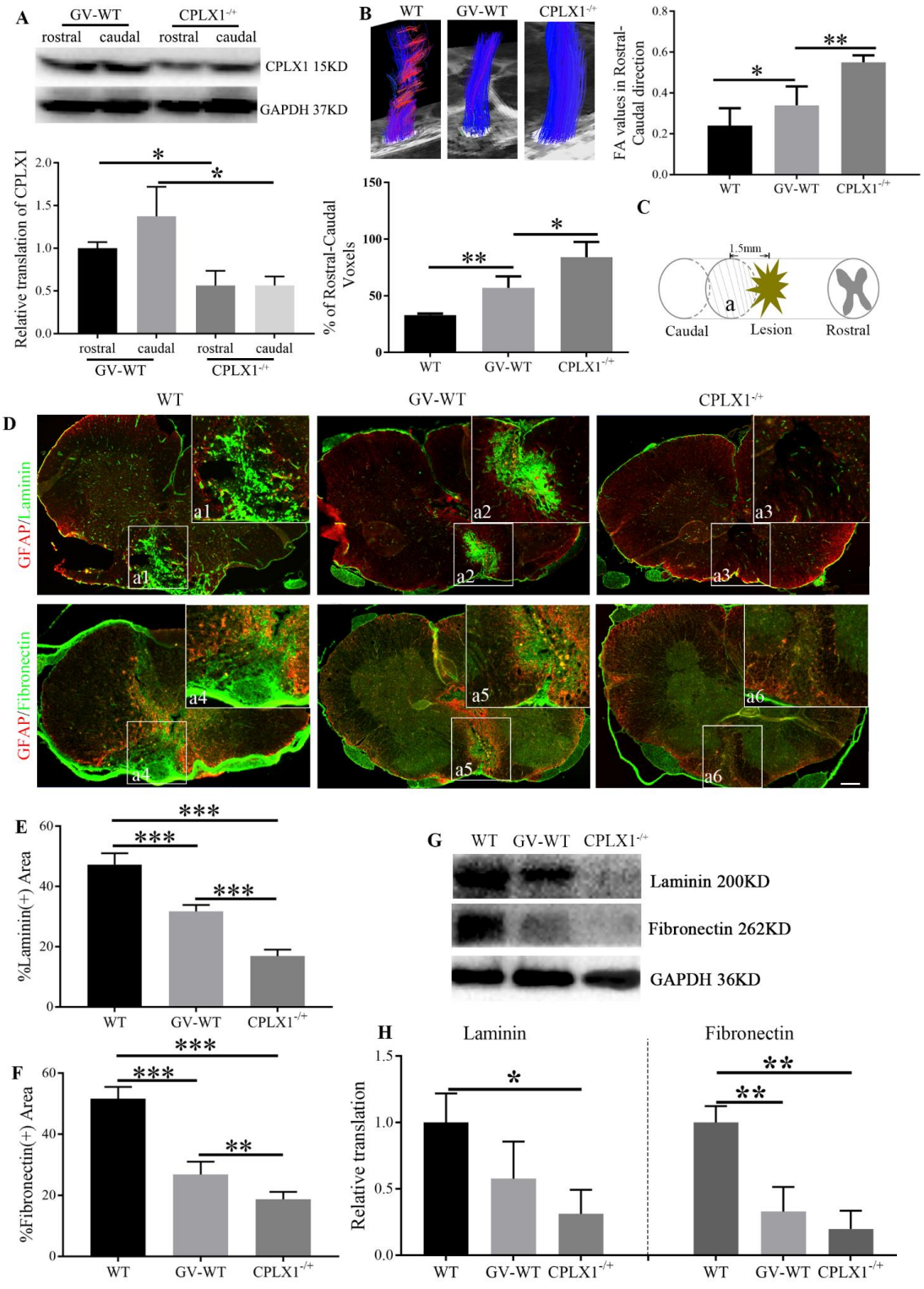

Figure 3. Moderate reduction of CPLX1 (CPLX1$^{-/+}$) enhances neural tissue regeneration and reduces fibrotic scar tissue after SCC even more than GV application. (**A**) WB of CPLX1 in the candal and rostral spinal cord extracts among GV treatment group (GV-WT) and CPLX1$^{-/+}$ group (n = 3 animals per group). (**B**)

Typical fiber tract reconstruction for the wild-type SCC (WT), GV-WT and CPLX1$^{-/+}$ groups is displayed. Graph of averaged FA values and percentages of rostral–caudal voxel numbers of the three groups in the area rostral and caudal 5mm to the lesion site (n = 4-6 animals per group). (**C**) Diagram illustrating the spinal cord contusion and displayed region (labeled as a) in the following figure 2D. (**D**) Immunolabeling of laminin, fibronectin and glial fibrillary acidic protein (GFAP) in transverse section in the indicated section marked in figure 2C (labeled as a) among these three groups. Scale bar: 200 μm. (**E and F**) GFAP- and Fibronectin-positive (+) area at the lesion site (n = 5 animals per group). (**G and H**) WB of laminin and fibronectin in caudal spinal cord extracts (n = 3 animals per group). Data were analyzed using a one-way ANOVA followed by a Bonferroni's post hoc test. Values are plotted as means ± SEM. *P < 0.05, **P < 0.01, ***P < 0.001.

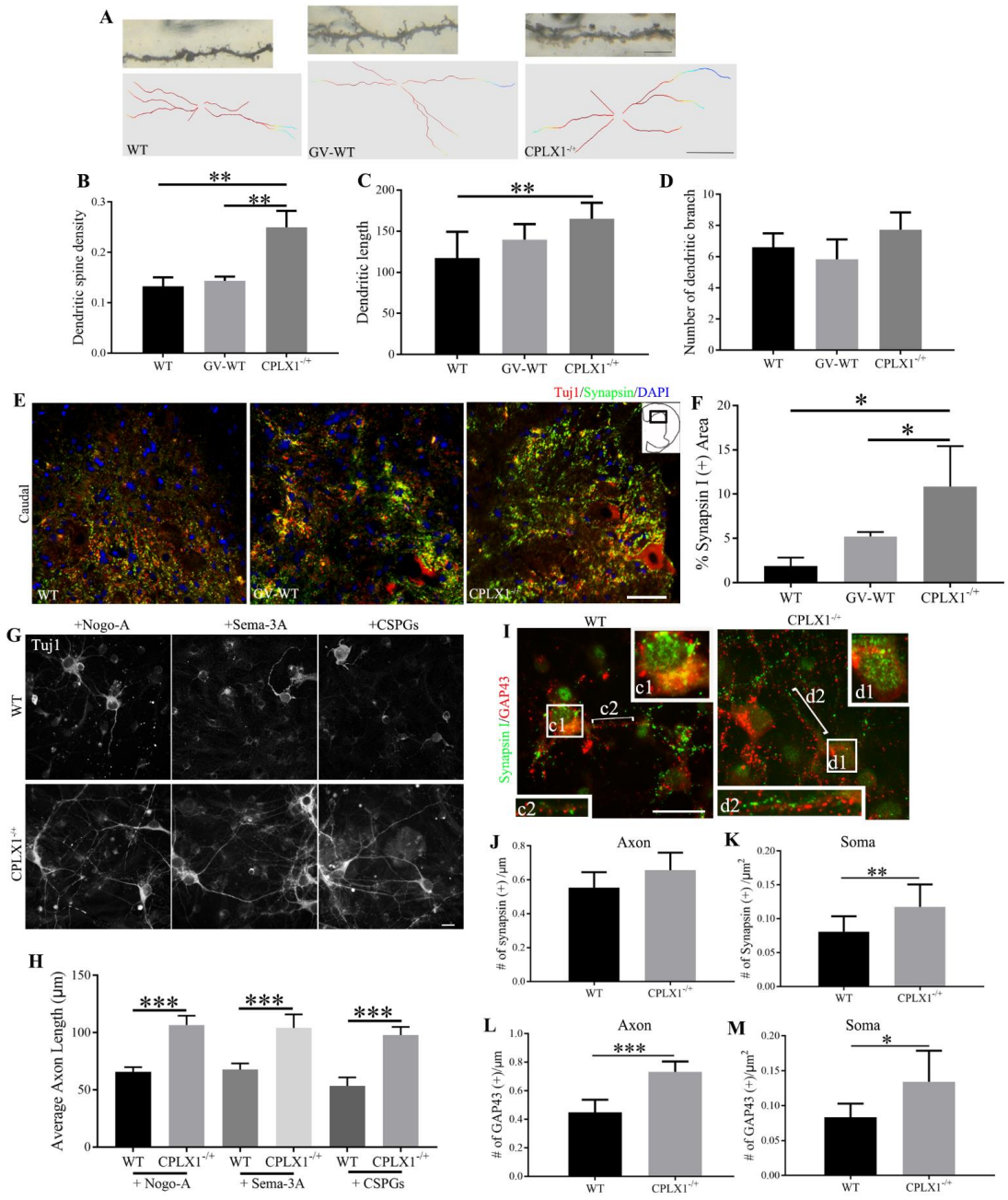

Figure 4. Moderate reduction of CPLX1 (CPLX1$^{-/+}$) enhances synaptic plasticity and axon elongation in cortical neurons with increased GAP43 expression. (**A**) Reconstructions of anterior horn motor neurons of caudal spinal cord in WT, GV-WT and CPLX1$^{-/+}$ group show different dendritic patterns and dendritic spine density. Scale bar in the top panel: 5μm； Scale bar in the bottom panel: 50μm. (**B**) Quantitative data of dendritic spine density (n = 3 animals per group). (**C**) Quantitative data of dendritic length (n = 3 animals per group). (**D**) Quantitative data of dendritic branch (n = 3 animals per group). (**E**) Double immunolabeling of synapsin I (green) with Tuj1 (red).

Scale bar: 50μm. (**F**) Quantitative data of synapsin I positive area (n = 3-4 animals per group). (**G**) Beta-3 tubulin (Tuj-1) immunolabeling of neurons growing on inhibitory substrates (Nogo-A; Sema-3A, Semaphorin-3A; CSPGs, chondroitin sulfate proteoglycans). Scale bar: 10μm. (**H**) Neurite length of cortical neurons after 48 hours in WT and CPLX1$^{-/+}$ genotype (n = 6 wells per group). (**I**) Double immunolabeling of synapsin (green) with neuronal GAP43 (red). Boxed region in the low magnification image on the centre is shown at higher magnification immediately to the periphery. Scale bar: 10μm. (**J and K**) Quantification of synapsin immunoreactivity at the axon and neuronal soma (n = 6 wells per group). (**L and M**) Quantification of GAP43 immunoreactivity at the axon and neuronal soma (n = 6 wells per group). Student's t-test was used for statistics between 2 groups. Three or more groups of data were analyzed using a one-way ANOVA followed by a Bonferroni's post hoc test. Values are plotted as means + SEM. *P < 0.05, **P < 0.01, ***P < 0.001.

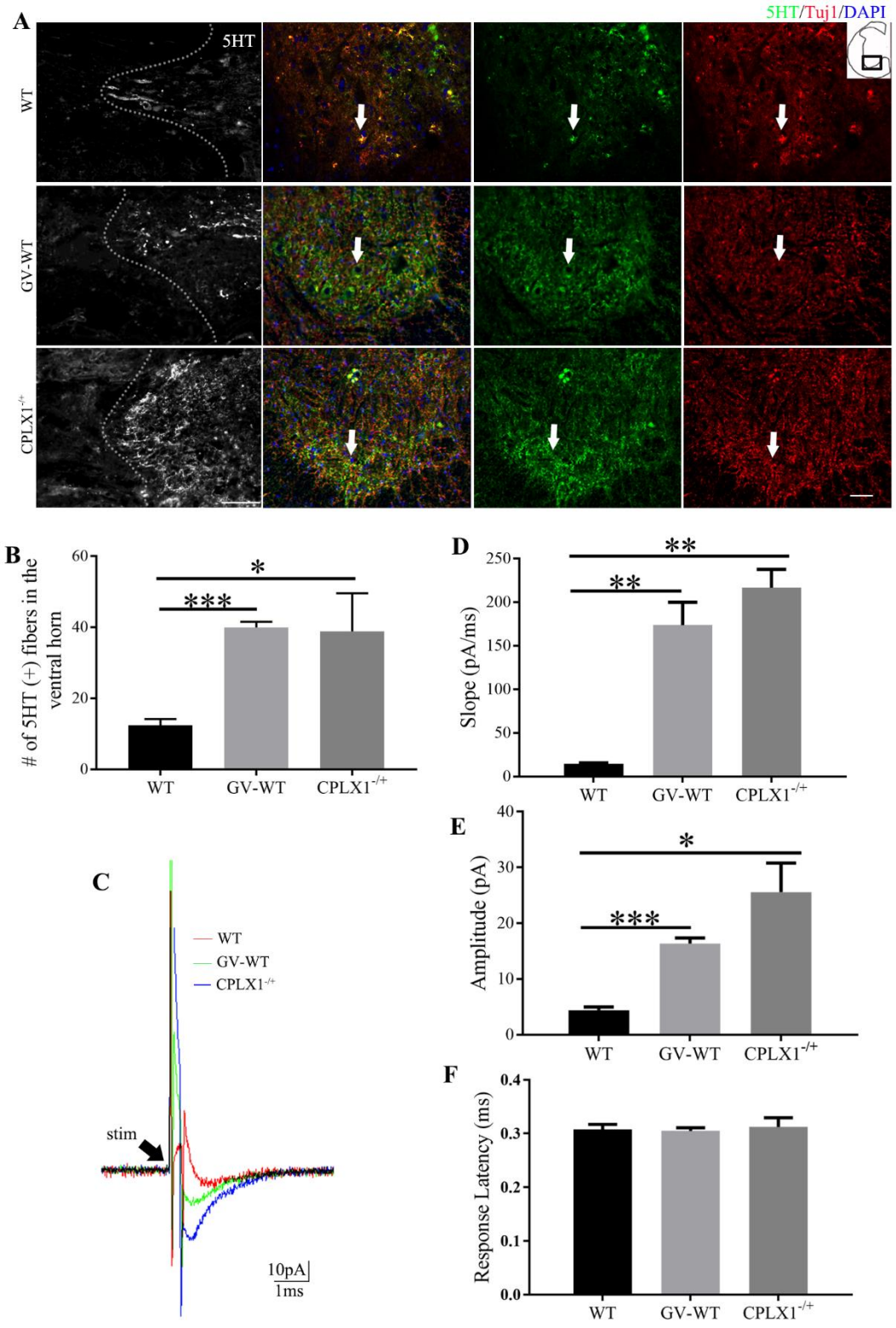

Figure 5. Moderate reduction of CPLX1 (CPLX1$^{-/+}$) promotes regeneration of serotonergic spinal axons, and increases the fEPSP caudal to the lesion even more than GV application. (**A**)Serotonin (5HT) immunolabeling (dashed line, lesion border) and longitudinal sections of the rat lumbar spinal cord after contusion injury. The

second panel, double-staining of 5HT and Tuj1 in the transverse section of caudal spinal cord. The third and fourth panel, images of each marker visualizing serotonergic innervation of motor neurons (arrows). Scale bar in the first panel: 100μm and in the last panel: 50μm. (**B**) The number of 5HT labeled (+) fibers caudal to a rat spinal cord (n =3-5 animals per group). (**C**) Representative traces of averaged (30 trials) DC evoked fEPSCs from 4 weeks WT (red trace), GV-WT (green trace) and CPLX1$^{-/+}$ (blue trace) SCC rat. (**D**) Quantitative data show the charge for evoked responses in three groups (n =5 animals per group). (**E**) Group comparisons for dorsal column evoked peak amplitude (n =5 animals per group). (**F**) Group comparisons for dorsal column evoked response latency (n =5 animals per group). Data were analyzed using a one-way ANOVA followed by a Bonferroni's post hoc test. Values are plotted as means + SEM. *P < 0.05, **P < 0.01, ***P < 0.001.

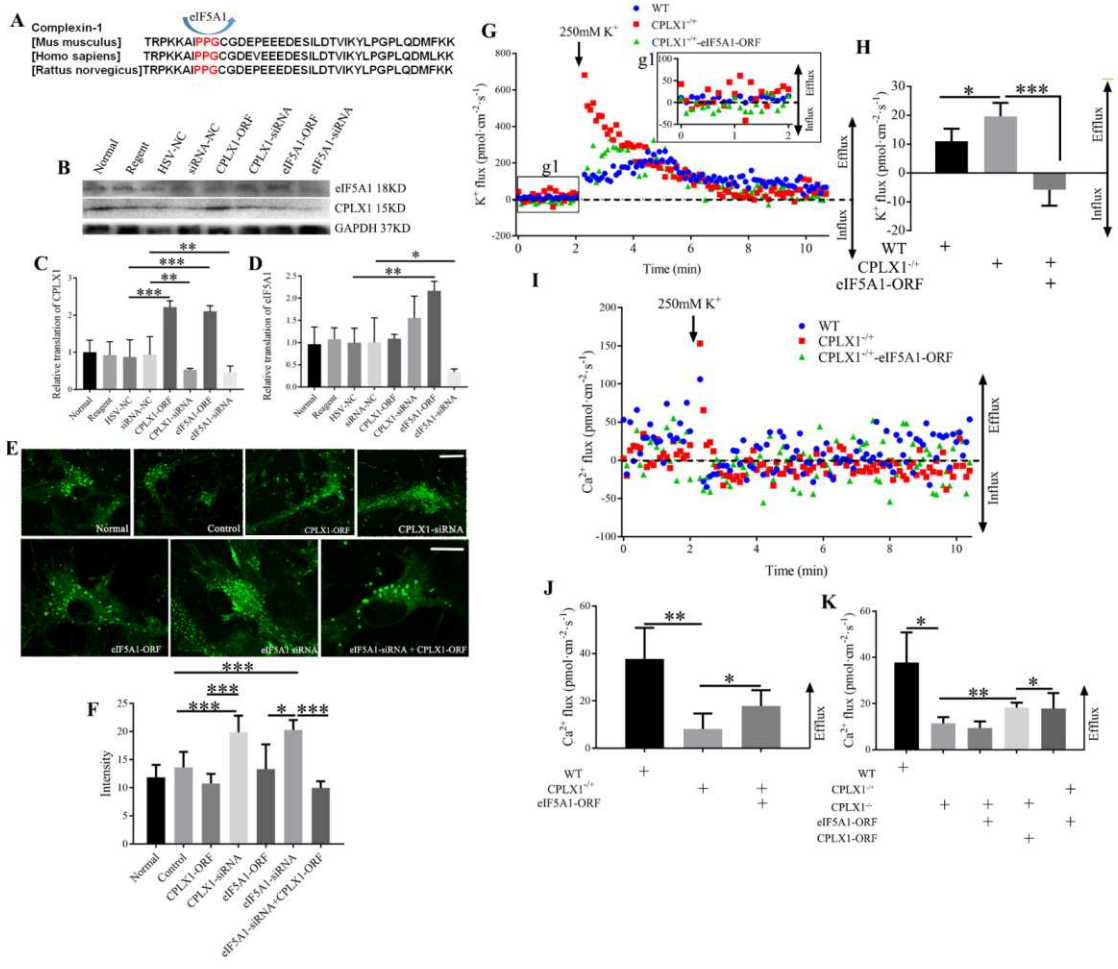

Figure 6. eIF5A1 promotes CPLX1 expression. (**A**) Amino acid sequence contained

952 the PPG of CPLX1 in mouse, rat and human. (**B**) WB analysis of soluble proteins
953 extracted from different treated spinal cord neurons. GAPDH served as a loading
954 control. (**C**) Quantification of CPLX1 level among different groups (n =6 wells per
955 group). (**D**) Quantification of eIF5A1 level among different groups (n =6 wells per
956 group). (**E**) Exocytosis labeling by FM1-43 in cortical neurons processing differently.
957 Scale bar: 10μm. (**F**) Quantification of the fluorescence intensity among different
958 groups (n =6 wells per group). (**G**) K^+ ion flux of primary cultured spinal cord neurons
959 before and after high potassium treatment. Figure g1 showed the larger version of
960 baseline of K^+ ion flux. (**H**) Baseline of K^+ ion flux in WT or presence of either CPLX1^{-}
961 $^{/+}$ or transfected with HSV-eIF5A1-ORF (n =6 wells per group). (**I**) Ca^{2+} ion flux of
962 primary cultured spinal cord neurons before and after high potassium treatment. (**J and**
963 **K**) Baseline of Ca^{2+} ion flux among different groups (n =6 wells per group). Data were
964 analyzed using a one-way ANOVA followed by a Bonferroni's post hoc test. Data are
965 plotted as means ± SEM. *P < 0.05, **P < 0.05, ***P < 0.001.
966

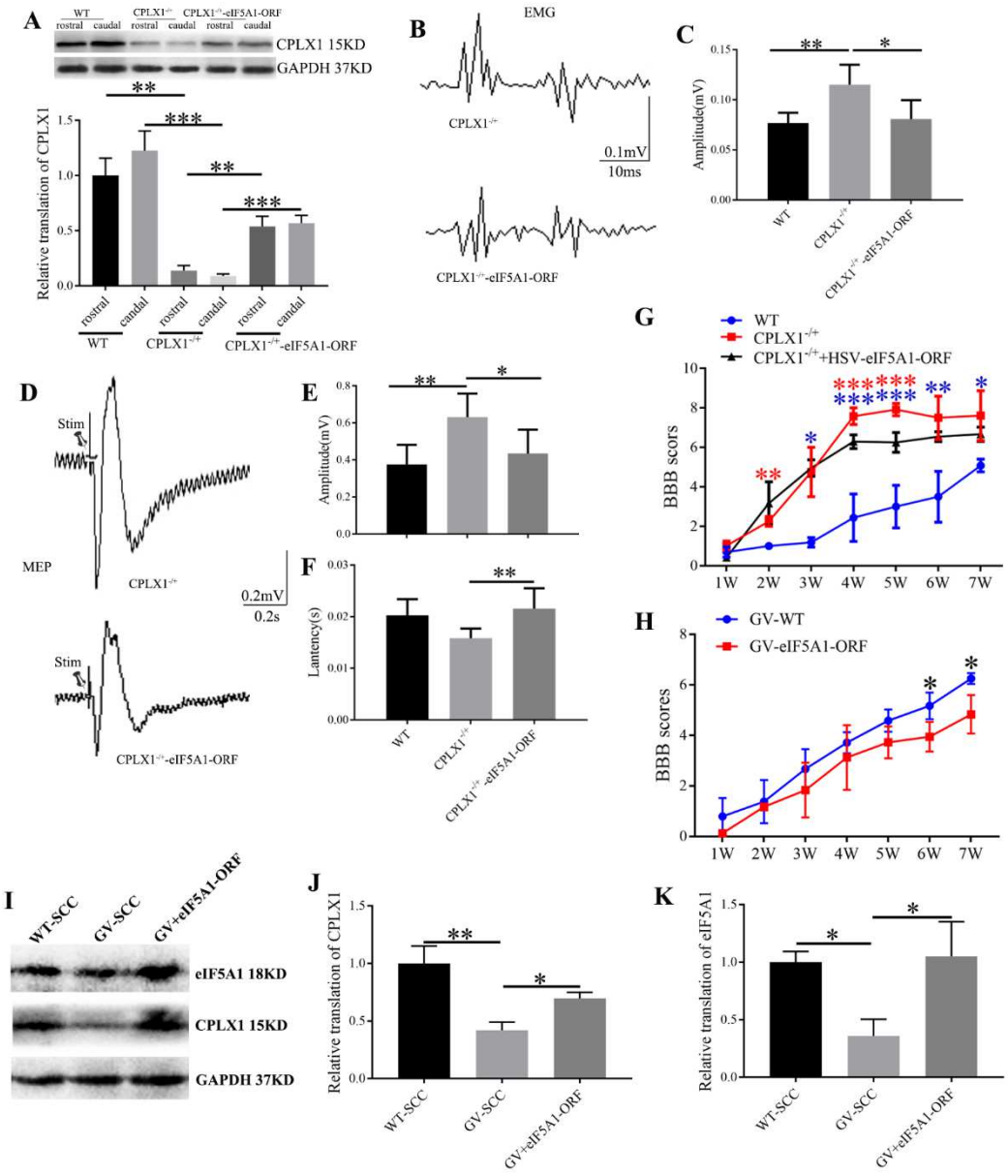

Figure 7. eIF5A1 regulates the function of CPLX1 in SCC models. (**A**) WB of CPLX1 in the caudal and rostral spinal cord extracts among different groups, n = 3 animals per group (n =3 rats per group). (**B**) Representative EMG signals in different group. (**C**) Quantification of amplitude among these indicated groups (n=4 animals per group). (**D**) Representative MEP signals in different group. (**E**) Quantification and statistical analyses of amplitude for the aforementioned experiments are shown (n=4 animals per group). (**F**) Quantification of latency period for these groups (n=4 animals per group). (**G and H**) BBB scores among these indicated group (n=6-8 animals per group). (**I**) WB of CPLX1 and eIF5A1 in the injured spinal cord extracts of GV-WT and GV+eIF5A1-ORF groups. (**J and K**) Quantification of eIF5A1 and CPLX1

978 translation among different groups (n=3-4 animals per group). Data were analyzed
979 using a one-way ANOVA followed by a Bonferroni's post hoc test. Data are plotted as
980 means ± SEM. *P < 0.05, **P < 0.05, ***P < 0.001.

Figures

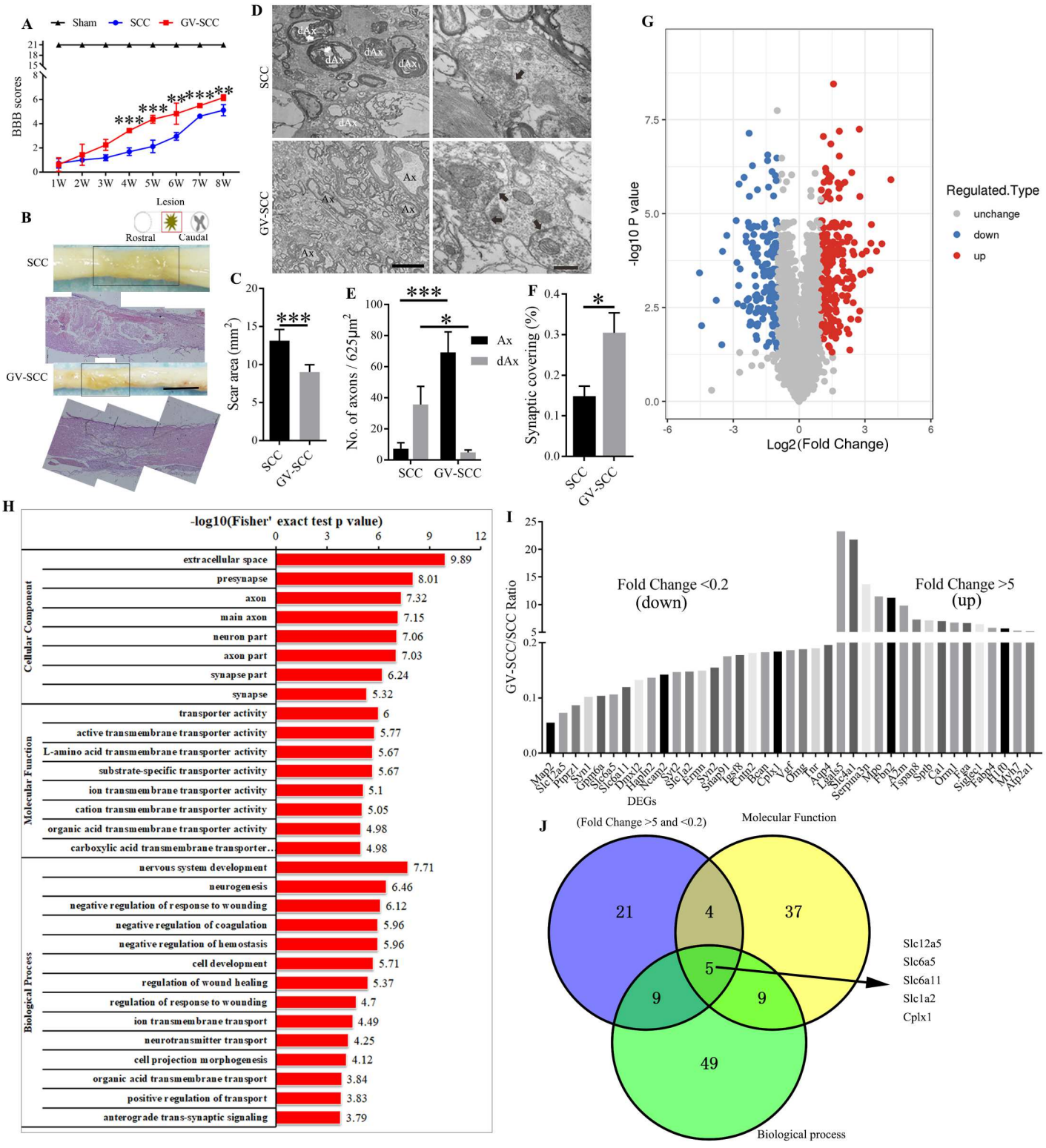

Figure 1

GV treatment accelerate the recovery of motor ability and increases synaptic plasticity after SCC which were related to down-regulating the expression of five candidates. (A) BBB scores of SCC and GV-SCC groups (n = 6–8 rats per group/time point). (B) Low power photographs and sagittal view of the spinal

cord of SCC and GV-SCC rats. Solid rectangles mark the injured area and the lower panels are the HE stain of lesion area. Scale bar: 500nm (C) Quantification of scar area of injured spinal cord in SCC rats with/without GV treatment (n = 6-8 mice per group). (D) Electron microscopic images of spinal cord sections rostral to the epicenter of the lesion in SCC rats and GV-treated rats. Arrows indicate presynaptic receptors contacting motor neuron surfaces. dAx: degenerating axon; Ax: myelinated axons. Scale bar in the left panel: 5μm Scale bar in the right panel: 500nm. (E) Number of different types of axons in the damaged penumbra (n = 5 rats per group (3 sections per animal)). (F) Percentage of motor neuron circumference covered by synapses within ventral horn (n = 5 rats per group (3 sections per animal)). (G) Volcano plot of all differentially expressed genes (DEGs) between lesion sites of SCC and GV-SCC animals at 4 wpi (n = 4-6 rats per group). The data for all genes are plotted as log2 fold change of the adjusted p-value. (H) GO functional enrichment analysis of DEGs. (I) Bar graph showing the DEGs sorted according to the fold change >5 or <0.2. (J) Three866 set venn diagram represent the selected DEGs according to the indicated strategy. Scheme in (B) indicates lesion and displayed region (red box). wpi, weeks post injury. Data were analyzed using Student's t-test. Values are plotted as means ± SEM. *P < 0.05, **P < 0.01, ***P < 0.001.

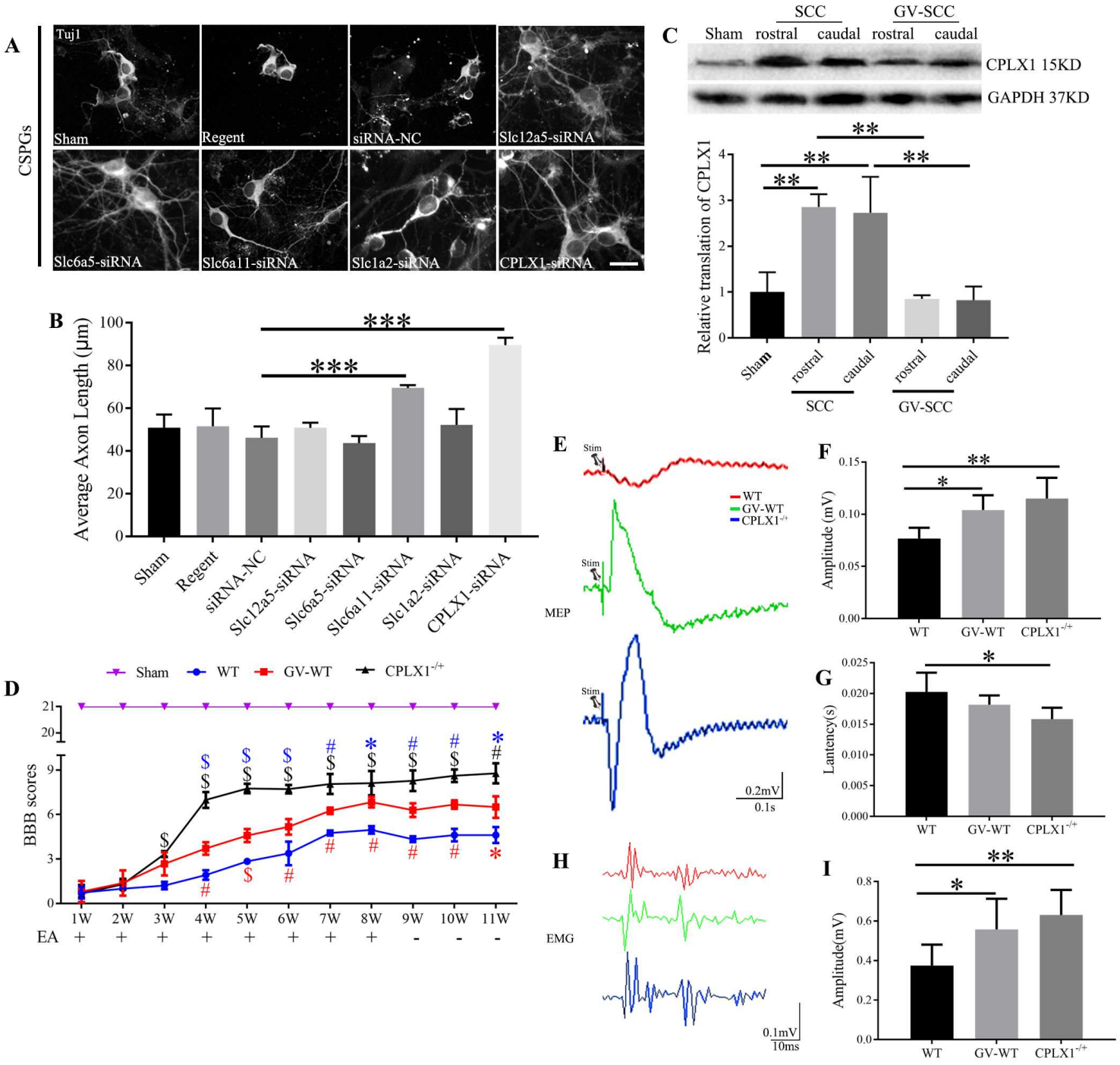

Figure 2

Moderate reduction of CPLX1 improve the MEP and EMG and enhances motor function of hind limbs simultaneously after SCC even more than GV application. (A) Beta-3 tubulin (Tuj-1) immunolabeling of neurons growing on inhibitory substrates (CSPGs, chondroitin sulfate proteoglycans) among different groups. Scale bar: 5μm. (B) Quantification of neurite length of cortical neurons under different conditions (n = 6 wells per group). (C) Western blots (WB) of CPLX1 in regions of rostral and caudal to the epicenter (n=3 animals per group). (D) BBB scores of the aforementioned experiments are shown (n=6-8 animals per group). Red symbols represent GV-WT group vs. WT group at corresponding time point; black symbols represent CPLX1-/+ group vs. WT group at corresponding time point; Blue symbols represent

CPLX1-/+group vs. GV-WT group at corresponding time point; *P<0.05, #P<0.01, $ P<0.001. (E) The figure shows representative MEP signal in different group. (F) Quantification and statistical analyses of amplitude for the aforementioned experiments are shown (n=4 animals per group). (G) Quantification of latency period for these groups (n=44 animals per group). (H) Representative EMG signal in different group. (I) Quantification of amplitude for these groups (n=4 animals per group). Data were analyzed using a one-way ANOVA followed by a Bonferroni's post hoc test. *P < 0.05, **P < 0.01, ***P < 0.001 in figure B, C, F, G and I. Values are plotted as means ± SEM.

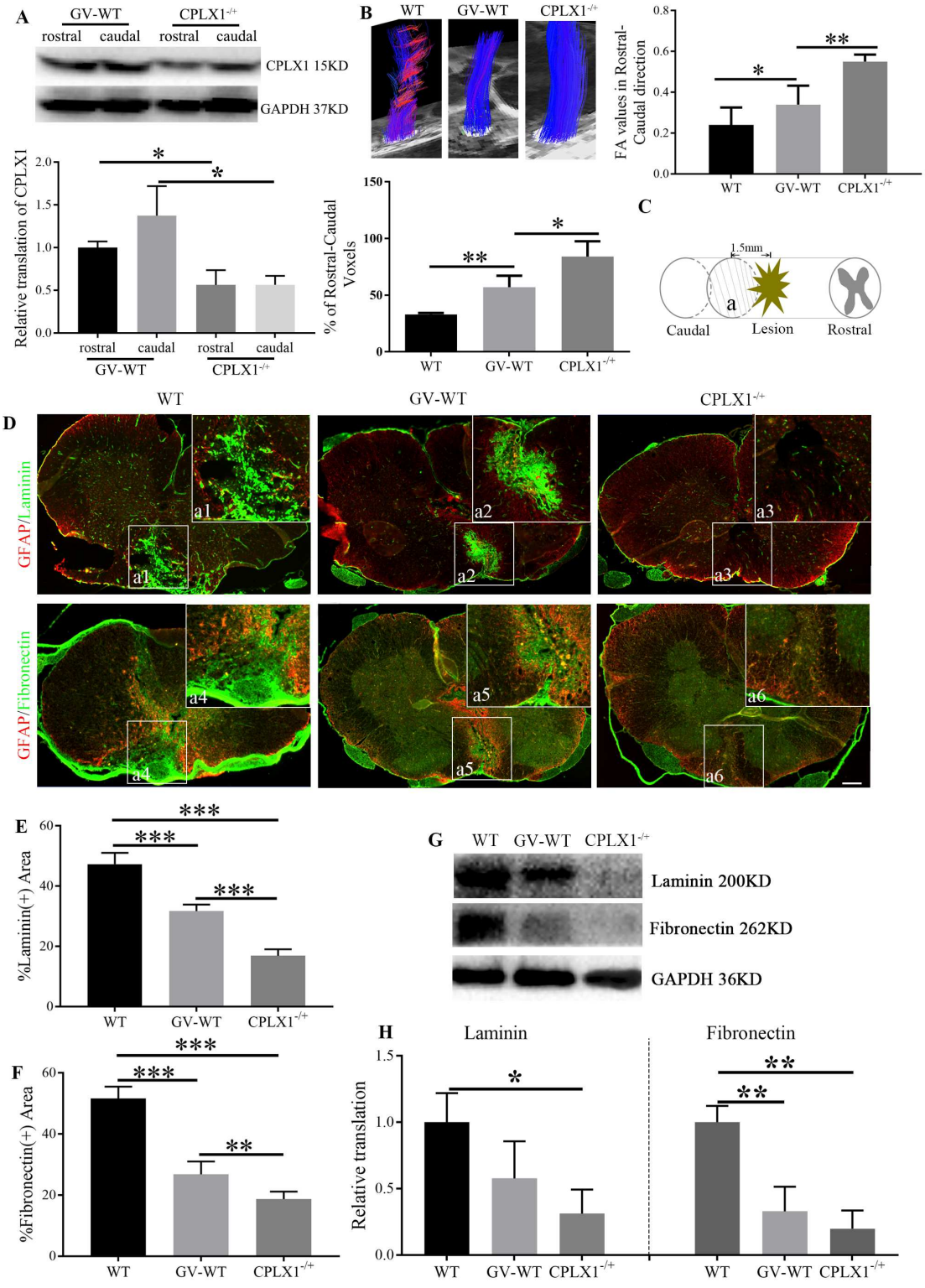

Figure 3

Moderate reduction of CPLX1 (CPLX1-/+) enhances neural tissue regeneration and reduces fibrotic scar tissue after SCC even more than GV application. (A) WB of CPLX1 in the candal and rostral spinal cord extracts among GV treatment group (GV-WT) and CPLX1-/+ group (n = 3 animals per group). (B) Typical fiber tract reconstruction for the wild-type SCC (WT), GV-WT and CPLX1-/+ groups is displayed. Graph of averaged FA values and percentages of rostral–caudal voxel numbers of the three groups in the area rostral and caudal 5mm to the lesion site (n = 4-6 animals per group). (C) Diagram illustrating the spinal cord contusion and displayed region (labeled as a) in the following figure 2D. (D) Immunolabeling of laminin, fibronectin and glial fibrillary acidic protein (GFAP) in transverse section in the indicated section marked in figure 2C (labeled as a) among these three groups. Scale bar: 200 μm. (E and F) GFAP- and Fibronectin-positive (+) area at the lesion site (n = 5 animals per group). (G and H) WB of laminin and fibronectin in caudal spinal cord extracts (n = 3 animals per group). Data were analyzed using a one-way ANOVA followed by a Bonferroni’s post hoc test. Values are plotted as means ± SEM. *P < 0.05, **P < 0.01, ***P < 0.001.

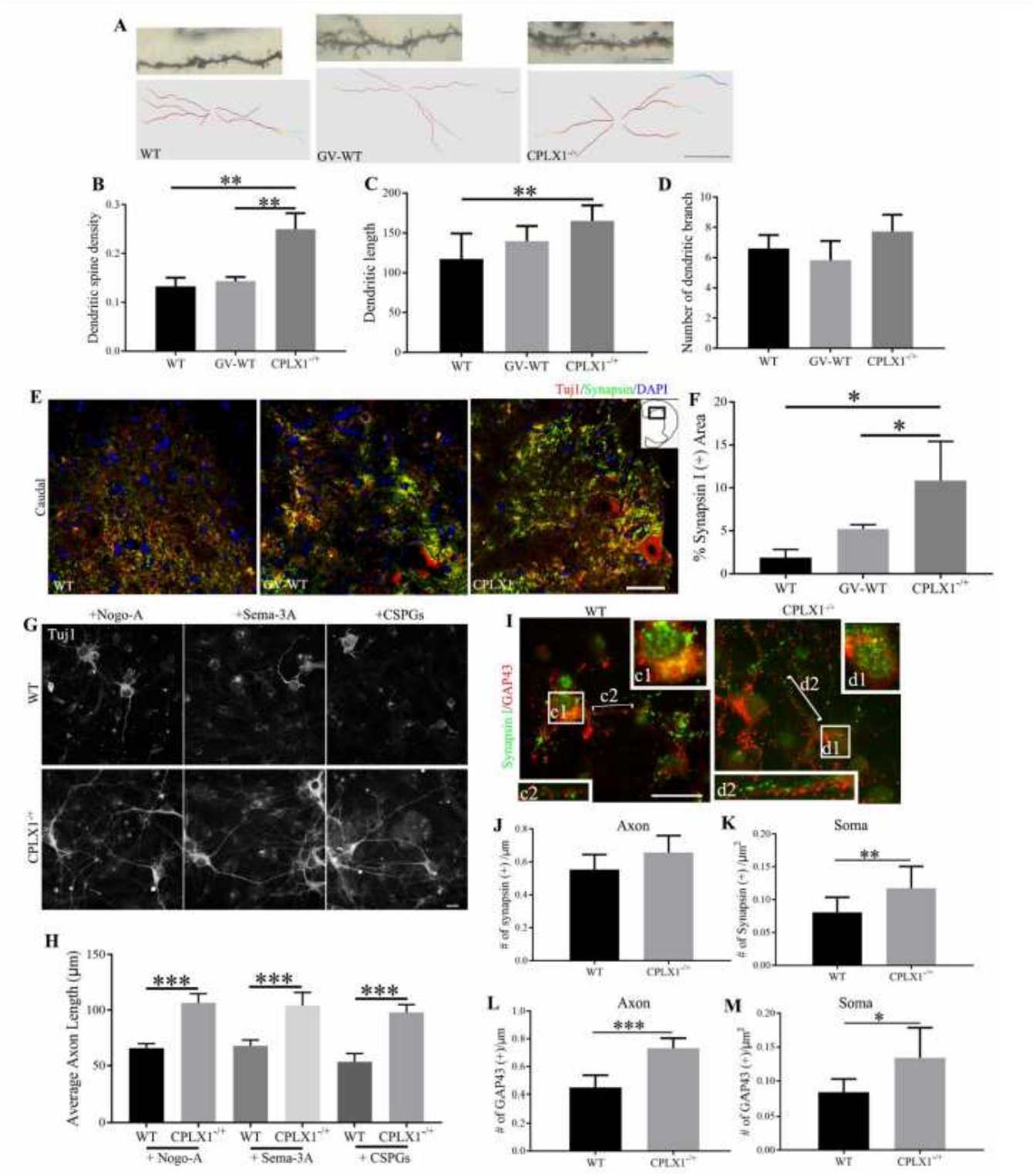

Figure 4

Moderate reduction of CPLX1 (CPLX1-/+) enhances synaptic plasticity and axon elongation in cortical neurons with increased GAP43 expression. (A) Reconstructions of anterior horn motor neurons of caudal spinal cord in WT, GV-WT and CPLX1-/+ group show different dendritic patterns and dendritic spine density. Scale bar in the top panel: 5μm Scale bar in the bottom panel: 50μm. (B) Quantitative data of dendritic spine density (n = 3 animals per group). (C) Quantitative data of dendritic length (n = 3 animals

per group). (D) Quantitative data of dendritic branch (n = 3 animals per group). (E) Double immunolabeling of synapsin I (green) with Tuj1 (red). Scale bar: 50μm. (F) Quantitative data of synapsin I positive area (n = 3-4 animals per group). (G) Beta-3 tubulin (Tuj-1) immunolabeling of neurons growing on inhibitory substrates (Nogo-A; Sema-3A, Semaphorin-3A; CSPGs, chondroitin sulfate proteoglycans). Scale bar: 10μm. (H) Neurite length of cortical neurons after 48 hours in WT and CPLX1-/+ 922 genotype (n = 6 wells per group). (I) Double immunolabeling of synapsin (green) with neuronal GAP43 (red). Boxed region in the low magnification image on the centre is shown at higher magnification immediately to the periphery. Scale bar: 10μm. (J and K) Quantification of synapsin immunoreactivity at the axon and neuronal soma (n = 6 wells per group). (L and M) Quantification of GAP43 immunoreactivity at the axon and neuronal soma (n = 6 wells per group). Student's t test was used for statistics between 2 groups. Three or more groups of data were analyzed using a one-way ANOVA followed by a Bonferroni’s post hoc test. Values are plotted as means + SEM. *P < 0.05, **P < 0.01, ***P < 0.001.

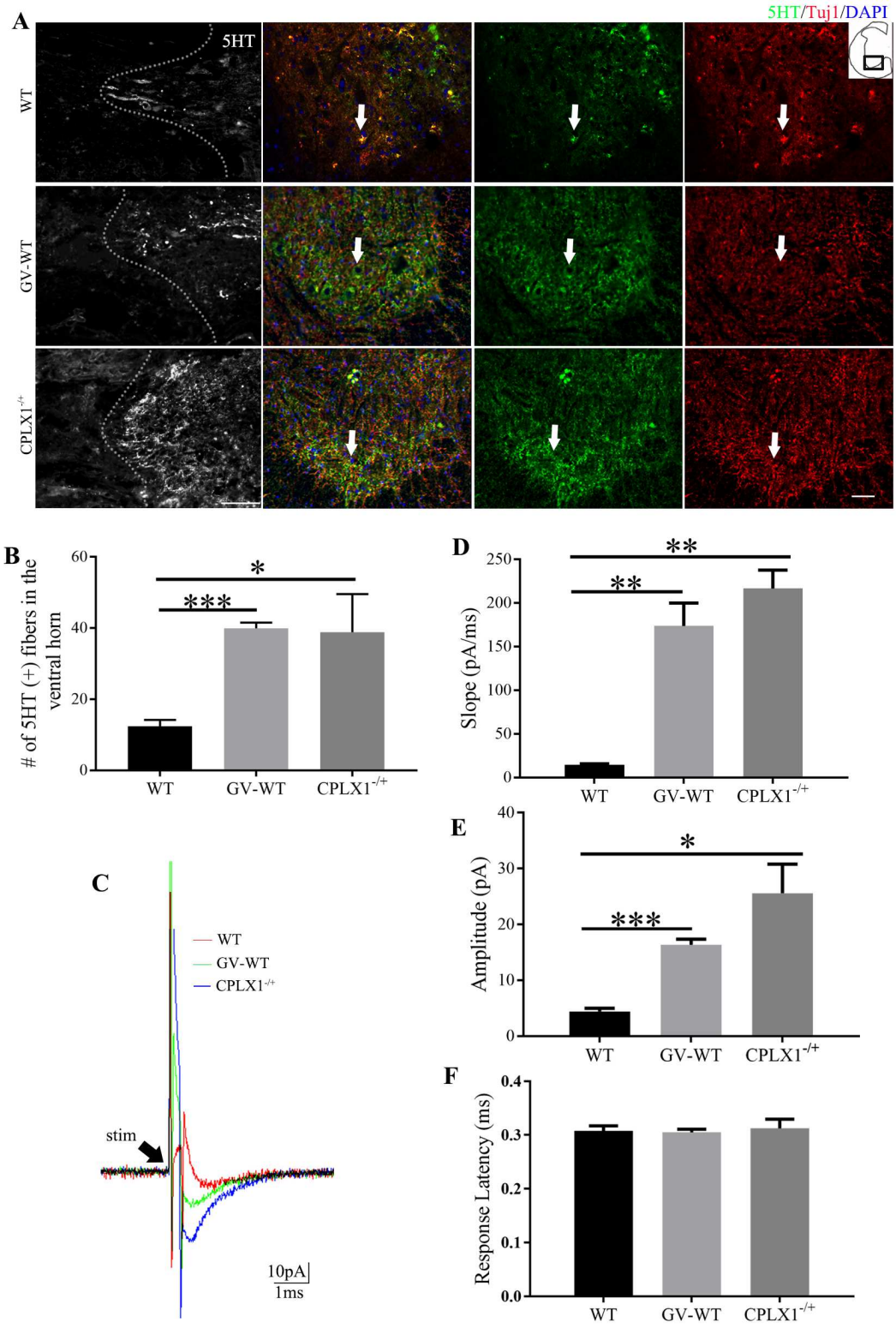

Figure 5

Moderate reduction of CPLX1 (CPLX1-/+) promotes regeneration of serotonergic spinal axons, and increases the fEPSP caudal to the lesion even more than GV application. (A)Serotonin (5HT) immunolabeling (dashed line, lesion border) and longitudinal sections of the rat lumbar spinal cord after contusion injury. The second panel, double-staining of 5HT and Tuj1 in the transverse section of caudal spinal cord. The third and fourth panel, images of each marker visualizing serotonergic innervation of

motor neurons (arrows). Scale bar in the first panel: 100μm and in the last panel: 50μm. (B) The number of 5HT labeled (+) fibers caudal to a rat spinal cord (n =3-5 animals per group). (C) Representative traces of averaged (30 trials) DC evoked fEPSCs from 4 weeks WT (red trace), GV-WT (green trace) and CPLX1-/+ (blue trace) SCC rat. (D) Quantitative data show the charge for evoked responses in three groups (n =5 animals per group). (E) Group comparisons for dorsal column evoked peak amplitude (n =5 animals per group). (F) Group comparisons for dorsal column evoked response latency (n =5 animals per group). Data were analyzed using a one-way ANOVA followed by a Bonferroni's post hoc test. Values are plotted as means + SEM. *P < 0.05, **P < 0.01, ***P < 0.001.

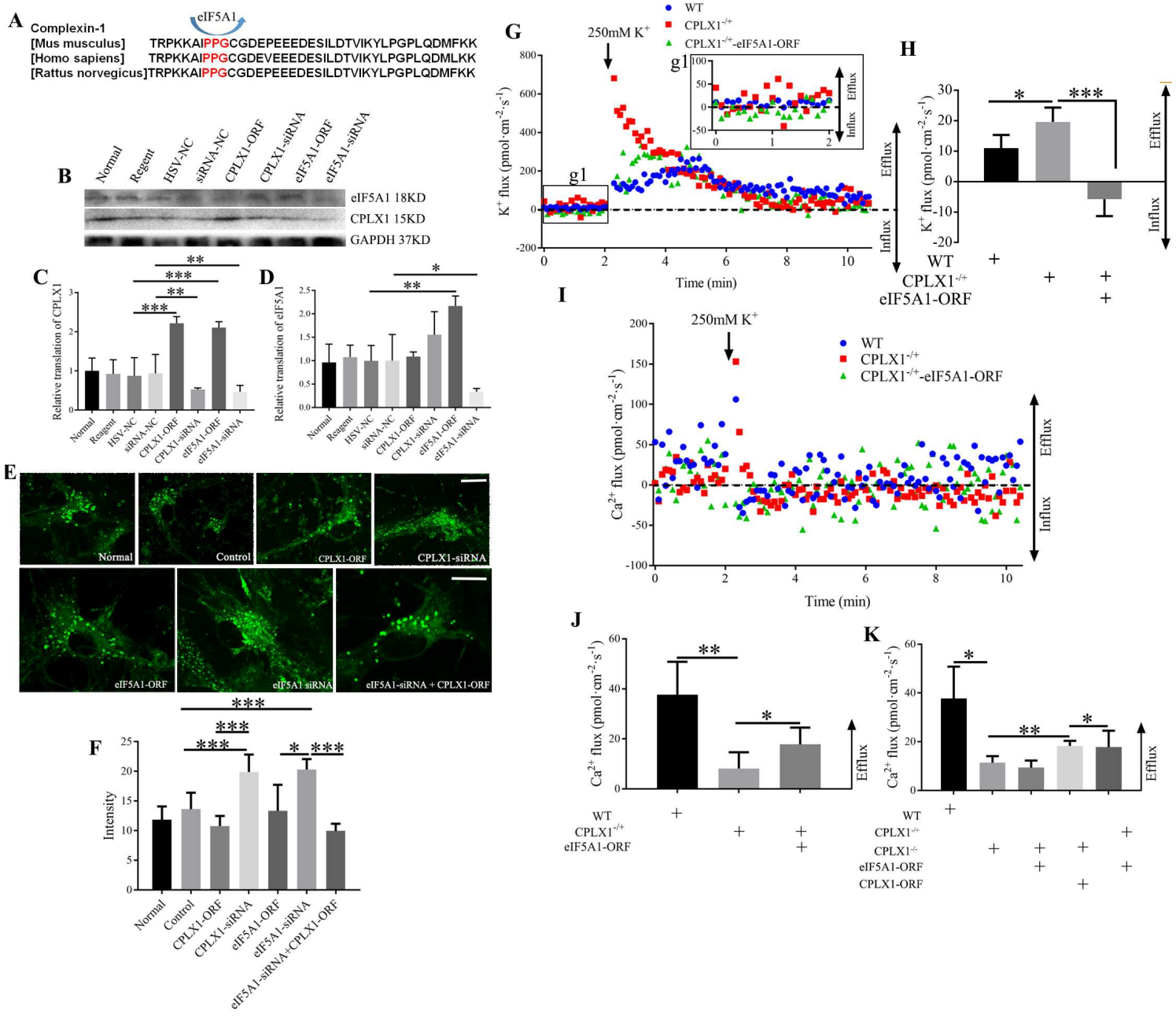

Figure 6

eIF5A1 promotes CPLX1 expression. (A) Amino acid sequence contained the PPG of CPLX1 in mouse, rat and human. (B) WB analysis of soluble proteins extracted from different treated spinal cord neurons.

GAPDH served as a loading control. (C) Quantification of CPLX1 level among different groups (n =6 wells per group). (D) Quantification of eIF5A1 level among different groups (n =6 wells per group). (E) Exocytosis labeling by FM1-43 in cortical neurons processing differently. Scale bar: 10μm. (F) Quantification of the fluorescence intensity among different groups (n =6 wells per group). (G) K + ion flux of primary cultured spinal cord neurons before and after high potassium treatment. Figure g1 showed the larger version of baseline of K+ ion flux. (H) Baseline of K+ ion flux in WT or presence of either CPLX1- /+ or transfected with HSV-eIF5A1-ORF (n =6 wells per group). (I) Ca2+ 961 ion flux of primary cultured spinal cord neurons before and after high potassium treatment. (J and K) Baseline of Ca2+ ion flux among different groups (n =6 wells per group). Data were analyzed using a one-way ANOVA followed by a Bonferroni's post hoc test. Data are plotted as means ± SEM. *P < 0.05, **P < 0.05, ***P < 0.001.

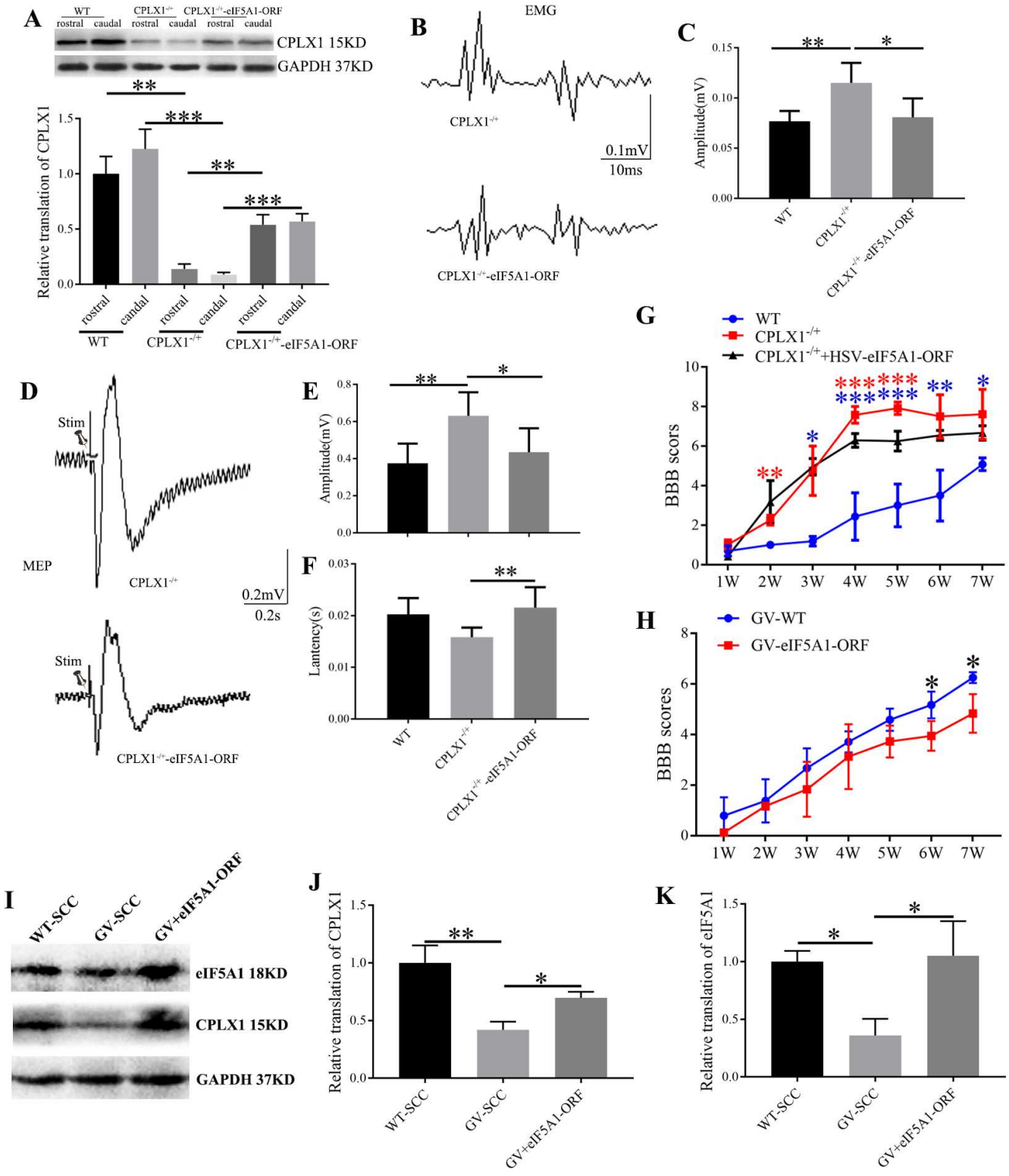

Figure 7

eIF5A1 regulates the function of CPLX1 in SCC models. (A) WB of CPLX1 in the caudal and rostral spinal cord extracts among different groups, n = 3 animals per group (n =3 rats per group). (B) Representative EMG signals in different group. (C) Quantification of amplitude among these indicated groups (n=4 animals per group). (D) Representative MEP signals in different group. (E) Quantification and statistical analyses of amplitude for the aforementioned experiments are shown (n=4 animals per group). (F)

Quantification of latency period for these groups (n=4 animals per group). (G and H) BBB scores among these indicated group (n=6-8 animals per group). (I) WB of CPLX1 and eIF5A1 in the injured spinal cord extracts of GV-WT and GV+eIF5A1-ORF groups. (J and K) Quantification of eIF5A1 and CPLX1 translation among different groups (n=3-4 animals per group). Data were analyzed using a one-way ANOVA followed by a Bonferroni's post hoc test. Data are plotted as means ± SEM. *P < 0.05, **P < 0.05, ***P < 0.001.

Supplementary Files

This is a list of supplementary files associated with this preprint. Click to download.

- supplementalmaterial.docx
- nrreportingsummary11.pdf
- SupplementalFigure6.tif
- SupplementalFigure2.tif
- SupplementalFigure1.tif
- SupplementalFigure3.tif
- SupplementalFigure4.tif
- SupplementalFigure5.tif